Extending satellite ocean color remote sensing to the near-blue ultraviolet bands

Yongchao Wang,[1] Zhongping Lee,[2,*] Jianwei Wei,[2,3,4] Shaoling Shang,[1] Menghua Wang,[3] Wendian Lai [1]

[1] Xiamen University, State Key Laboratory of Marine Environmental Science, Xiamen, 361102, China

[2] School for the Environment, University of Massachusetts Boston, Boston, MA 02125, USA

[3] NOAA Center for Satellite Applications and Research, Marine Ecosystems and Climate Branch, College Park, MD 20740, USA

[4] Global Science & Technology Inc., Greenbelt, MD 20770, USA

* Corresponding email address: zhongping.lee@umb.edu

Abstract:

Ultraviolet (UV) radiation has a profound impact on marine life, but historically and even currently, most ocean color satellites cannot provide radiance measurements in the UV, and thus UV penetration, in the global ocean. We develop a system (termed as $UVISR_{dl}$) in this study, based on deep learning, to estimate remote sensing reflectance (R_{rs}) at 360, 380, and 400 nm (collectively termed as near-blue UV bands, nbUV) from R_{rs} in the visible bands that are obtained by ocean color satellites. This system is tested using both synthetic and field-measured data that cover a wide range and large number of values, with the resulted coefficient of determination close to 1.0 and bias close to 0 between $UVISR_{dl}$ estimated and known R_{rs}(nbUV). These results indicate excellent predictability of R_{rs}(nbUV) from R_{rs}(visible) via $UVISR_{dl}$. The system was further applied to VIIRS (the Visible Infrared Imaging Radiometer Suite) data with the estimated R_{rs}(nbUV) evaluated using matchup field measurements, and obtained a mean absolute relative difference (MARD) at 360 nm of ~14% for oceanic waters and ~50% for coastal waters. These results are equivalent to those reported in the literature for satellite R_{rs}(visible) in oceanic and coastal waters. Examples of the global distribution of R_{rs}(nbUV), and subsequently the diffuse attenuation coefficient at the nbUV bands (K_d(nbUV)), are generated after applying $UVISR_{dl}$ to R_{rs}(visible) from the VIIRS data. The system lays the groundwork to generate decade-long R_{rs}(nbUV) and K_d(nbUV) from satellite ocean color data, which will be useful and important for both ocean color remote sensing and biogeochemical studies.

1. Introduction

Ultraviolet (UV) radiation is part of solar energy, which plays complex roles in biogeochemical processes on land and in ocean (Cullen and Neale 1994; Smith et al. 1992; Zepp et al. 2007). For instance, high doses of UV can inhibit the growth of plants and phytoplankton, while low doses under some conditions can be a useful energy source for phytoplankton photosynthesis (Gao et al. 2012). In addition, phytoplankton may develop mycosporine-like amino acids (MAAs) in response to UV radiation; these MAAs are strongly UV absorbing, functioning as a "shield" to protect photosynthesis pigments (Moisan and Mitchell 2001; Morrison and Nelson 2004). Further, dissolved organic matter (DOM) has a high absorption capacity for UV radiation and undergoes photochemical conversion under sunlight, indicating that DOM is very sensitive to sunlight in the UV domain (Piccini et al. 2009; Zepp et al. 2007). UV radiation may also impact the diel vertical movement of zooplankton (Rose et al. 2012). In the atmosphere, since the most absorbing aerosol species contribute absorption in the shorter (UV-visible) wavelengths (Kahn et al. 2016), research on UV radiation will also help improve atmospheric correction (Frouin et al. 2019). As indicated in Werdell et al. (2018), the future use of hyperspectral spectrometer from UV (~350 nm) to near-infrared (~900 nm) will improve the accuracy in ocean color remote sensing. All these suggest the necessity to map UV penetration in the global ocean.

The distribution of underwater UV radiation depends on two factors: UV intensity at the sea surface and the diffuse attenuation coefficients for downwelling irradiance (K_d; m^{-1}) at these UV wavelengths. The first factor is governed by ozone and atmospheric properties, which can now be well estimated using satellite measurements (Herman and Celarier 1997; Kuchinke et al. 2004; Smyth 2011b; Vasilkov et al. 2001). K_d is an apparent optical property of the ocean; although there are many field measurements (Conde et al. 2000; Dupouy et al. 2018; Overmans and Agustí 2019; Tedetti and Sempéré 2006) and more than four decades of K_d(visible) from ocean color satellites, there is no standard global K_d(UV) product distributed by the remote sensing agencies. This is in part because the shortest wavelength of the past and most of the present-day ocean color satellites is ~410 nm. Thus, there are no global measurements of oceanic optical properties in the UV domain by satellites. Two decades ago, Vasilkov et al. (2001) presented a preliminary oceanic distribution of UV radiation in the 280-320 nm range based on TOMS (the Total Ozone Mapping Spectrometer) and SeaWiFS (the Sea-viewing Wide Field-of-view Sensor) products, but the empirical coefficients for the K_d(UV) model were not derived from globally inclusive measurements. Thus its applicability to the global ocean is unknown. In short, the penetration of UV radiation in the global ocean is still far from known, nor the impact of UV radiation on marine life on a basin scale. Only some recent ocean color satellite sensors and the planned PACE (Plankton, Aerosol, Cloud and ocean Ecosystem, US) include bands in the UV domain. For instance, the OLCI (Ocean and Land Colour Instrument, Europe) on Sentinel 3 has a band at 400 nm, SGLI (Second Generation Global Imager, Japan) has one at 380 nm, HY1C (HaiYang-1C, China) has one at 355 nm, and PACE will have hyperspectral measurements starting from 350 nm.

The model to estimate K_d(UV) used in Vasilkov et al. (2001) is based on the "Case 1" concept (Morel 1988). The authors evaluated K_d at 313, 320, 340, and 380 nm with 15 measurements from the CalCOFI cruises and obtained an uncertainty of ~20%. Similarly, to fill the information gap of K_d in the UV domain, based on ~50-100 measurements made in the Mediterranean Sea and Atlantic Ocean, Smyth et al. (2011b) proposed empirical relationships to estimate K_d at 305, 325, 340, and 380 nm using the total absorption coefficient at 443 nm (a(443), m^{-1}). Because K_d is dominated by the absorption coefficient (Gordon 1989a), these approaches require the absorption coefficient of colored dissolved organic matter (CDOM) to co-vary with the concentration of chlorophyll (Chl), but such a correlation is not always strong even for oceanic waters (Kahru and Mitchell 1998; Lee and Hu 2006). As pointed out by Smyth et al. (2011b), the correlation is actually weak between a(443) and K_d(305). This may not be a surprise, as very different relationships have been found between K_d(310) and K_d(465) for different waters (Højerslev and Aas 1991), and significantly different K_d(UV) exists between waters of the Mediterranean Sea and South Pacific for the same Chl (Morel et al. 2007). Thus, the applicability of such empirical schemes in the global ocean is limited, although global Chl, a(443), and K_d(490) are adequately available from satellite ocean color measurements.

In a separate empirical approach, Fichot et al. (2008) developed algorithms to estimate K_d of 320, 340, and 380 nm based on the SeaWiFS bands after principal component analysis, with the 335 data points used for the algorithm development covering waters from the Gulf of Mexico to many other coastal regions around North America. This algorithm was later refined to improve the estimates of inshore waters (Cao et al. 2014). While promising results were reported (Cao et al. 2014; Fichot et al. 2008), basin-scale UV penetration, which is of the most significance, remains unknown.

Another approach to obtain K_d(UV) is to extrapolate the inherent optical properties (IOPs) obtained in the visible bands to UV and then estimate K_d(UV) through models developed based on the radiative transfer equation (Lee et al. 2005). This approach requires *a priori* information of the relationships of component IOPs in the UV to the visible domain, which could be weak. For instance, the existence of MAAs may contribute significantly to the phytoplankton absorption coefficient (a_{ph}) in the short UV wavelengths, while MAAs may have very low or no absorption in the visible domain (Moisan and Mitchell 2001; Shick and Dunlap 2002); thus, there is no clear indication of MAAs' existence from a_{ph} in the visible. Also, the approach will require a robust estimate of the spectral shape parameter (S_g; nm^{-1}) of CDOM absorption coefficient (a_g) (Swan et al. 2013; Twardowski et al. 2004), as a_g could be significantly higher in the UV domain (Mannino et al. 2008; Morel and Gentili 2009) and S_g may also vary with spectral range (Twardowski et al. 2004). All estimates of these components will bring various levels of uncertainty to K_d(UV).

Given the issues mentioned above, we present a scheme centered on deep learning to estimate remote sensing reflectance (R_{rs}; sr^{-1}) in the near-blue UV domain (nbUV hereafter) from R_{rs} in the visible (~410-700 nm), with nbUV specifically for 360, 380, and 400 nm. The reason for the shortest wavelength as 360 nm is in part because UV radiation for wavelengths shorter than ~350 nm is extremely low (Vantrepotte and Mélin 2006); in part because there is no clear relationship between a_{ph}(λ<350 nm) and a_{ph}(visible) (Dupouy et al. 1997; Morrison and Nelson 2004; Sathyendranath et al. 1987), where the contribution from MAAs could play a significant role for the short UV wavelengths (Moisan and Mitchell 2001; Shick and Dunlap 2002); and because more advanced ocean color satellites start measurements around 350 nm. However, these factors do not forbid the development of systems from estimating R_{rs} for wavelengths shorter than 360 nm after a better understanding of the relationships between IOPs of wavelengths shorter than 360 nm and those in the visible bands.

It is certainly possible to develop a deep-learning-based system to estimate K_d(nbUV) from K_d(visible), as K_d(visible) can be adequately calculated from R_{rs}(visible) (Lee et al. 2013; Lee et al. 2005). We decided not to take this approach here because R_{rs} is the core input to estimate water properties and because R_{rs}(nbUV) can also be applied in some atmospheric correction algorithms (He et al. 2012; Wang 2007). In addition, R_{rs}(nbUV) can be used to improve the inversion of a_{ph} and a_g in ocean color remote sensing (Wei and Lee 2015; Wei et al. 2016). Furthermore, as an additional option for cross-validation, R_{rs}(nbUV) in oceanic waters obtained from MODIS (the Moderate Resolution Imaging Spectroradiometer) and/or VIIRS (the Visible Infrared Imaging Radiometer Suite) can be used to compared with those from OLCI, SGLI, and/or HY1C.

The paper is organized as follows. In Section 2, we describe the overall deep-learning architecture for estimating R_{rs}(nbUV), and the data used to train and evaluate the system. In Section 3, results and evaluations are presented. In Section 4, we show applications of this system in the global ocean. In Section 5, we summarize our main findings and present future perspectives.

2. Data and methods

2.1 A deep-learning system for R_{rs}(nbUV): UVISR$_{dl}$

For easy data processing, especially because of nonlinear relationships of R_{rs} between different wavelengths, we take an approach centered on deep learning for estimating R_{rs}(nbUV) from R_{rs}(visible). Figure 1 presents a schematic concept of this system, termed UVISR$_{dl}$.

Like all deep-learning systems, UVISR$_{dl}$ is composed of one input layer, various hidden layers associated with many numbers of neurons, and one output layer. A key component of any deep-learning system is the neural network model, and such models have been developed in the past decade (Abadi et al. 2016; Géron 2019; Ketkar 2017; Steiner et al. 2019; Swami and Jain 2011). Here, based on data characteristics, we selected the Keras model (Chollet) for UVISR$_{dl}$. Keras is a deep-learning Application Programming Interface written in Python; it is publicly available and running on top of the machine-learning platform TensorFlow (Chollet ; Ketkar 2017). The number of hidden layers and the number of neurons of each layer were determined following the concept of minimum loss (Géron 2019), a common approach for developing a deep-learning system. Eventually, a system of four hidden layers, with 300 neurons for Layer-1, 75 for Layer-2, 38 for Layer-3, and 18 for Layer-4, is found to provide the best performance for $\mathrm{UVISR_{dl}}$.

For the training of $\mathrm{UVISR_{dl}}$, we employed the Rectified Linear Unit (ReLu) function for the activation function of each layer (Krizhevsky et al. 2012), which can largely avoid gradient explosion and gradient disappearance (He et al. 2015). The optimization function of the training used is the Adam algorithm (Kingma and Ba 2014). The setting of the learning rate usually involves an adjustment process, in which the highest possible learning rate is manually selected (Zeiler 2012). As a result, a learning rate of 2×10^{-5} is used in this study. Training of $\mathrm{UVISR_{dl}}$ was eventually achieved when the loss function converges and the iteration stops.

To avoid any interference between the nbUV wavelengths, a separate $\mathrm{UVISR_{dl}}$ was trained specifically for each of the three nbUV bands in this effort. Further, given different spectral band settings of satellite ocean color sensors, separate $\mathrm{UVISR_{dl}}$ was developed for each specific satellite of interest.

2.2 Data

For all neural networks or deep-learning schemes, a large and inclusive dataset is crucial for its training. Here, we use numerically synthesized data to develop $\mathrm{UVISR_{dl}}$, which is further evaluated using both synthesized and field-measured data.

2.2.1 Training data

Following IOCCG Report #5 (IOCCG-OCAG 2003; IOCCG 2006), we synthesized a large (200,000 sets) dataset containing a wide range of IOPs in the 350-800 nm range (5-nm resolution), which were then fed into a model for R_{rs} (Lee et al. 2004) to generate 200,000 R_{rs} spectra. As most of the specifics for this synthesizing method are available in the literature

(IOCCG-OCAG 2003; IOCCG 2006), we provide only some of the components and synthesizing steps in Appendix A for reference. A few key features are summarized below:

(1) For the IOPs spectra, while the contributions of pure seawater (Lee et al. 2015a; Mason et al. 2016; Zhang and Hu 2009a) are considered constants, the absorption and backscattering contributions from phytoplankton pigments, CDOM, and detrital-sediments are considered variables. These component IOPs, except for the spectrum of a_{ph}, can be expressed as a simple function (exponential or power-law) of wavelength (Bricaud et al. 1981; Gordon and Morel 1983). Therefore, to best maintain the natural variation of bulk IOPs, a_{ph} spectra were not modeled mathematically; instead, they were selected from >4,000 a_{ph} spectra stored in the SeaBASS (the Sea-viewing Wide Field-of-view Sensor Bio-Optical Archive and Storage System) and our own collections. To ensure coverage from oligotrophic oceanic waters to coastal/inland eutrophic waters, we set $a_{\mathrm{ph}}(440)$ to a range of 0.001-20.0 m^{-1}. Therefore, a wide range of $a_{ph}(\lambda)$, in both magnitude and spectral shapes, were utilized in data synthesizing.

(2) As described in Appendix A and IOCCG Report #5 (IOCCG-OCAG 2003; IOCCG 2006), for each $a_{\mathrm{ph}}(440)$ value, constrained random parameters were used to model the contributions of other component IOPs. In this way, it better mimics the variabilities of these components in natural environments while reducing likely unrealistic combinations, such as very low $a_{\mathrm{ph}}(440)$ with an extremely high absorption by CDOM.

Figure 2a shows examples of the synthesized R_{rs} spectra. The dataset of 200,000 IOPs-R_{rs} is divided randomly by an 8:2 ratio, with 160,000 for the training of UVISR$_{\mathrm{dl}}$ and 40,000 for the evaluation of UVISR$_{\mathrm{dl}}$. Table 1 provides an overall picture of the data range used for the evaluation. Visible bands used are 410, 440, 490, 550, and 670 nm for VIIRS, 410, 440, 490, 510, 555, and 670 nm for SeaWiFS, and 410, 440, 490, 530, 550, and 670 nm for MODIS. The spectral bands of these satellite sensors have a bandwidth of 10-20 nm, and the band centers are not exactly those specified here. Thus, to apply the trained UVISR$_{\mathrm{dl}}$ for R_{rs} products from satellites, R_{rs} of the satellite bands were calculated for the 200,000 sets of hyperspectral R_{rs} after applying each satellite sensor's band-specific response functions. Subsequently, for example, nonlinear empirical conversions were developed to transfer VIIRS R_{rs} of band 411 nm to $R_{rs}(410)$, which was also done for the other bands. Therefore, for each satellite, the same $UVISR_{dl}$ can be applied to both field and satellite R_{rs}.

2.2.2 Validation data

In addition to the above-mentioned synthesized data for the validation of $UVISR_{dl}$, a wide range of field-measured R_{rs} are also used to test the performance of $UVISR_{dl}$. Figure 2b shows examples of measured R_{rs} spectra (from a total of 202), which cover waters from oceanic to turbid coastal regions. Details of the method for these measurements can be found in Wei et al. (2015), where the skylight-blocked approach (SBA) (Lee et al. 2013; Tanaka et al. 2006) was followed to obtain field R_{rs}. The uncertainty of SBA-measured R_{rs} is generally <5% in oceanic waters, and ~10% in turbid, highly productive waters at the blue bands (Lin et al. 2020). While the SBA measurements mostly cover coastal waters, the hyperspectral (344-749 nm, ~0.5-nm resolution) R_{rs} data measured at the Marine Optical Buoy (MOBY) (Clark et al. 1997), a typical oligotrophic site, were also accessed (from the NOAA CoastalWatch, https://www.star.nesdis.noaa.gov/socd/moby/filtered_spec/) to evaluate $UVISR_{dl}$. The quality of the MOBY data is classified into four classes: bad and cloudy, suspicious, bad, and good. In this study, we used 6,184 R_{rs} spectra with the highest quality.

2.3 Accuracy Assessment

In addition to the coefficient of determination (R^2) in linear regression analysis, the accuracy of the resulted R_{rs}(nbUV) is assessed with the following statistical measures: root-mean-square difference (RMSD), mean absolute relative difference (MARD), and bias. They are defined as follows:

$$\mathrm{RMSD} = \sqrt{\frac{\sum_{i=1}^{N}(X_{\mathrm{est,i}} - X_{\mathrm{mea,i}})^2}{\mathrm{N}}}, \tag{1}$$

$$\mathrm{MARD} = \frac{1}{\mathrm{N}}\sum_{i=1}^{N}\frac{|X_{\mathrm{est,i}} - X_{\mathrm{mea,i}}|}{X_{\mathrm{mea,i}}}, \tag{2}$$

$$\mathrm{bias} = \frac{1}{\mathrm{N}}\sum_{i=1}^{N}(X_{\mathrm{est,i}} - X_{\mathrm{mea,i}}), \tag{3}$$

where $X_{\mathrm{est,i}}$ and $X_{\mathrm{mea,i}}$ are predicted and known (synthesis, or *in situ*) values of R_{rs}(nbUV), respectively, and N is the number of sample pairs.

3. Results of R_{rs}(nbUV) from UVISR$_{dl}$

3.1 Synthetic data

R_{rs}(nbUV) from UVISR$_{dl}$ is first evaluated using the 40,000 synthetic data, with results for VIIRS spectral settings showing in Figure 3 (*a*-*c*) as examples. Similar results were obtained for SeaWiFS and MODIS, with statistical measures given in Table 2. Generally, for these synthesized data, the values of R^2 for the three wavelengths and three satellites are all close to 1.0, with values of RMSD and bias close to 0 and values of MARD under ~0.3%. These results indicate extremely high accuracy in predicting R_{rs}(nbUV) from R_{rs} data in five or six visible bands. This is due to the fact that R_{rs} is determined by the total absorption and backscattering coefficients. Because the spectral variations of CDOM absorption and particle backscattering are highly spectrally related, and because the spectral shapes of phytoplankton absorption show general patterns at least in the 350-700 nm domain, thus R_{rs}(visible) has some spectral "messages" or connections with R_{rs} at 360, 380, and 400 nm, although such spectral connections are likely more complex than that can be explained by simple nonlinear functions. This spectral interconnection was demonstrated in Lee et al. (2014) and Sun et al. (2015), where R_{rs} spectrum in the 400-800 nm with a resolution of 5 nm could be well constructed from R_{rs} measured at 15 bands in this spectral domain. Also, decades ago Austin and Petzold (1990) showed K_d(visible) could be estimated to some degree from using K_d(490) alone.

We would like to emphasize that the relationships between R_{rs}(nbUV) and R_{rs}(visible) of the synthesized dataset are complex and nonlinear, as presented in Figure 4. As a validation of the synthesized data, Figure 4 also includes R_{rs} from field measurements (both SBA and MOBY), which shows that field data are well within the envelope of the synthesized R_{rs}. This comparison suggests that the synthesized dataset is inclusive, although some combinations of IOPs potentially may not exist or are extremely rare in natural aquatic environments. The two clusters between R_{rs}(nbUV) and R_{rs}(440) represent the impact of the two driving component IOPs on R_{rs} spectral shapes in the nbUV: a_{ph} and a_g. Specifically, for the ~350-440 nm range,

a_g increases exponentially with the decrease of wavelength, but a_{ph} generally decreases with the decrease of wavelength. Thus, for waters having higher contributions from a_g than from a_{ph}, $a(360)$ will be significantly higher for the same $a(440)$. Consequently, $R_{rs}(360)$ will be lower for the same $R_{rs}(440)$. This contrast represents a common situation in coastal waters (depth < 1,000 m), which will be shown later.

Because $R_{rs}(360)$ does not co-vary with $R_{rs}(440)$, these patterns show that uncertainty will be large if $R_{rs}(440)$ alone is used to predict R_{rs}(nbUV); and this uncertainty would increase if the gap between the target and reference wavelengths becomes wider. However, as shown earlier, the R^2 values are close to 1.0 when R_{rs}(visible) was fed into a deep-learning system to obtain R_{rs}(nbUV), indicating that nonlinear connections exist between R_{rs}(nbUV) and R_{rs}(visible) and that deep learning has the capability to capture such relationships, although not in an explicit way.

It is also interesting that although VIIRS has no band around 510-530 nm compared to SeaWiFS and MODIS, the statistical measures for the predicted R_{rs}(nbUV) from VIIRS R_{rs}(visible) are similar to that of the two earlier sensors. This result suggests that the band around 510-530 nm is not critical for estimating R_{rs}(nbUV) from R_{rs}(visible), at least for the data tested here.

3.2 Field-measured data

We further evaluated UVISR$_{\mathrm{dl}}$ using field-measured data, with Figure 5 (a-c) showing the results for SBA measurements and Figure 6 (a-c) for MOBY measurements, with the VIIRS spectral bands as examples. Performances of the two datasets for MODIS and SeaWiFS bands are included in Table 2. Similar to the performance of the synthetic dataset, for SBA measurements, the R^2 values for the three R_{rs}(nbUV) and three satellites are ~0.99, with RMSD and bias close to 0. The MARD values are ~2%, ~4%, and ~10% for 400, 380, and 360 nm, respectively, much higher than those of the synthesized data. The higher MARD values are not surprising for the following reasons: 1) the measured R_{rs} is never error-free; 2) the uncertainty in field measured R_{rs} is always around a few percent even under the best arrangement with SBA (Lin et al. 2020) and can be around 10% in the blue for highly absorbing waters (Lin et al. 2020); and 3) likely insufficient representation of natural R_{rs} in the synthesized data for the training of UVISR$_{dl}$, which could be refined in the future after obtaining more high-quality measurements of R_{rs}(UV-visible) in broad aquatic environments. The less than 10% MARD and close to 0 bias indicate highly reliable R_{rs}(nbUV) predicted by UVISR$_{dl}$ from R_{rs}(visible).

Excellent results are also found with MOBY-measured R_{rs} (see Figures 6a-6c), where the RMSD and bias are close to 0, and the MARD values are less than ~9% for the estimated R_{rs}(nbUV) by UVISR$_{dl}$. The R^2 value (0.88) for R_{rs}(360) is slightly lower than that of the SBA dataset, which is in part due to the much narrower range (~0.005-0.020 sr^{-1}) of R_{rs}(360) from a single site. On the other hand, it also indicates potentially larger uncertainties for wavelengths deeper in the UV domain, especially, as shown below, if MAAs are present. Note that a result of ~9% MARD for R_{rs}(360) is close to the highest accuracy that can be achieved in field measurements (Lin et al. 2020; Zibordi and Talone 2020).

3.3 Potential impact of absorption by MAAs

As we stated earlier, we set the shortest wavelength for R_{rs}(nbUV) at 360 nm, in part because that the absorption coefficient of MAAs in the 300-350 nm range can be significantly higher (for instance, up to a factor of ~4) than that at 440 nm (see Figure 1B in Moisan and Mitchell 2001). In particular, because MAAs have no or low contributions to a_{ph} in the visible, there is no clear relationship between a_{ph}(visible) and a_{ph}(300-350). On the other hand, MAAs may exist in many phytoplankton groups, particularly in dinoflagellates *L. polyedra* and *Phaeocystis Antarctica* (Moisan and Mitchell 2001; Vernet and Whitehead 1996). Thus, the spectral information of a_{ph} in the visible is insufficient to accurately predict a_{ph} in the 300-350 nm domain due to the potentially existence of MAAs. Consequently, errors in the estimated a_{ph}(300-350) will be propagated to the estimated total absorption and then R_{rs}(300-350). The empirical algorithms to estimate K_d in the wavelengths of ~320 nm using R_{rs} in the visible bands developed earlier (Fichot et al. 2008; Smyth 2011a; Vasilkov et al. 2001) likely did not encounter waters having strong MAAs, or the data used were dominated by strong absorption due to CDOM. Because K_d is primarily determined by the absorption coefficient, such empirical algorithms for the estimate of K_d(300-350) could result in larger uncertainties than those for wavelengths in the nbUV when MAAs are present.

For the a_{ph} spectra used in our data synthesizing, very few spectra show contributions of MAAs at 360 nm, where the $a_{\mathrm{ph}}(360)/a_{\mathrm{ph}}(440)$ ratio is 0.66±0.35, although it is in a range of 0.15-3.82. On the other hand, the ratio of $a_{\mathrm{g}}(360)/a_{\mathrm{g}}(440)$ is ~3.3 for an a_{g} slope of 0.015 nm^{-1}. That means for a situation $a_{\mathrm{ph}}(440) = a_{\mathrm{g}}(440)$, MAAs contribute to the most ~50% to a(360) when $a_{\mathrm{ph}}(360)/a_{\mathrm{ph}}(440)$ is also around 3.0. For most situations where $a_{\mathrm{ph}}(360)/a_{\mathrm{ph}}(440)$ is less than 1.0, the value of a(360) is dominated by that from a_{g}(360); thus, it is feasible to reasonably predict a(360) from a(visible), and then R_{rs}(360) from R_{rs}(visible). As would be expected, there could be larger uncertainties in the estimated R_{rs}(360) if there are strong contributions from MAAs while the contribution of a_{g} is secondary.

4. Application to ocean color satellites

4.1 Global R_{rs}(nbUV) from VIIRS

With the developed and validated UVISR$_{\mathrm{dl}}$, it is possible to generate global R_{rs}(nbUV) from past and current ocean color satellite measurements. For example, Figure 7 shows global distributions of R_{rs}(nbUV) predicted from VIIRS. Note that both NOAA CoastWatch (https://coastwatch.noaa.gov/cw/index.html) and NASA OBPG (https://oceancolor.gsfc.nasa.gov/) can provide consistent VIIRS ocean color products, but for easier spatial matchup with the products from SeaWiFS and MODIS, seasonal composites of R_{rs}(visible) from NASA OBPG were acquired and utilized here.

Not surprisingly, R_{rs}(nbUV) is very high in the open ocean, especially in the ocean gyres, a result of significantly low CDOM and phytoplankton in the oligotrophic ocean (Hu et al. 2012; Siegel et al. 2005). The predicted R_{rs}(nbUV) in the South Pacific Gyre (the star in Figure 7b) is ~0.022 sr^{-1}, which is consistent with that reported in Tedetti et al. (2010), although the years of measurements are different.

Expectedly, R_{rs}(nbUV) is significantly lower in coastal waters, but even for R_{rs}(360), it is higher than zero in many coastal regions (see Figure 8 for example). Such distributions suggest caution in assuming R_{rs}(nbUV) as zero in the process of atmospheric correction (He et al. 2012), where other approaches (Wang and Jiang 2018; Wei et al. 2020) could be used for the estimation of R_{rs} in the blue bands.

4.2 Evaluation of VIIRS R_{rs}(nbUV) with *in situ* measurements

We further compared R_{rs}(nbUV) from VIIRS with matchup *in situ* measurements (82 matchups for SBA, and 730 for MOBY) to assess the quality of R_{rs}(nbUV) estimated from satellite data. The SBA measurements were obtained mainly in coastal regions (see Figure 9 for locations of measurements) in the period of 2012-2019, with matchup limited to within ±5 hours and 3x3 VIIRS pixels between satellite and *in situ* measurements (Werdell and Bailey 2005). Figures 10 and 11(*a-f*) present scatterplots between predicted and measured R_{rs}(nbUV) for visual comparison, with statistical measures presented in Table 3. In view that neither *in situ* nor satellite R_{rs}(nbUV) can be considered as "truth," the mean absolute unbiased relative difference (MAURD) is calculated to check consistency between the two determinations.

$$\mathrm{MAURD} = \frac{1}{N}\sum_{1}^{N}\left|\frac{Data_1 - Data_2}{Data_1 + Data_2}\right| \times 2 \tag{4}$$

where $Data_1$ and $Data_2$ represent data from two independent determinations, respectively.

Overall, for these R_{rs}(nbUV) the MAURD values are between 0.31 (at 400 nm) and 0.40 (at 360 nm) for the SBA matchups, with biases of ~0.0002-0.0005 sr^{-1}. For the MOBY matchups, the MAURD values are around 0.12, with biases of ~0.00023-0.0012 sr^{-1}. Unsurprisingly, these measures are worse than those when evaluating R_{rs}(nbUV) using field-measured data, as there are other uncertainties and/or errors contributing to these differences, which include not-exact spatial-temporal matchup and uncertainties in atmospheric correction, especially in coastal waters (IOCCG 2010; Wang 2007). For these likely error sources related to satellite data, Figures 10 and 11 (*d-f*) include comparisons of the blue bands (410, 440, and 490 nm), where the MAURD values are ~0.21-0.29 and RMSD is ~0.0012 sr^{-1} for the SBA matchups, which are just slightly better than those of R_{rs}(nbUV). Note that there are a few stations where VIIRS R_{rs}(410, 440, 490) are much lower than the *in situ* R_{rs} measured by the SBA. As R_{rs}(nbUV) is estimated based on the values in the visible bands, such lower values from VIIRS will lead to lower values of R_{rs}(nbUV), which then contributes to higher MAURD at the nbUV bands, especially in the coastal waters. For the

MOBY matchups, a fixed location of oceanic waters, the MAURD values at the blue bands (410-490 nm) are just slightly better than those at the nbUV bands (360-400 nm), with the RMSD values around 0.0022 sr^{-1} for the wavelengths of 360-410 nm. The low R^2 value for these matchups results from the narrow dynamic range of the R_{rs} values, where the water properties of such a system do not vary significantly. Overall, because of the difficulties and uncertainties in spatial-temporal matching as well as atmospheric correction and these performance measures being similar to those reported in the literature when evaluating R_{rs} from ocean color satellites (Antoine et al. 2008; Mélin et al. 2016; Zibordi et al. 2009), these results indicate satisfactory R_{rs}(nbUV) from VIIRS, although it is certainly necessary to carry out more evaluations in the future.

4.3 K_d(nbUV) from ocean color satellites

After obtaining R_{rs}(nbUV) from VIIRS, it is then possible to estimate K_d(nbUV) semi-analytically following Lee et al. (2005). The total absorption (a) and backscattering (b_b) coefficients at the nbUV-visible bands will be derived first from R_{rs}(nbUV-Visible) using a semi-analytical algorithm (Lee et al. 2002; Wang et al. 2009; Werdell et al. 2013). Since K_d is a function of a and b_b (Gordon 1989b; Lee et al. 2005; Lee et al. 2013), it is then straightforward to calculate K_d(nbUV) when a(nbUV) and b_b(nbUV) are known. As an example, Figure 12 shows global distributions of K_d(360) and K_d(380) (with the Sun at zenith) derived from VIIRS for seasonal composite of October to December 2012. At the center of the South Pacific Gyre, K_d(360) is ~0.031 m^{-1}, and K_d(380) is around ~0.025 m^{-1} during this period, which show general consistency with those reported previously (Morel et al., 2007), although the field measurements were taken in Nov. 2004. As stated earlier, there are other algorithms developed to estimate K_d in the UV domain using R_{rs} in the visible (Fichot et al. 2008; Smyth 2011a; Vasilkov et al. 2001). It is thus important to evaluate the performances of these algorithms for the global ocean, which is out of the scope of this effort.

4.4 Further implications for the "Case 1" approach in oceanic waters

As aforementioned in the introduction, the earlier approaches (Højerslev and Aas 1991; Smyth 2011b; Tedetti et al. 2010; Vasilkov et al. 2005) estimated K_d(nbUV) using Chl or K_d (or a) at one visible band as the input, which is based on the "Case 1" concept proposed by Morel and Prieur (1977) decades ago, where the inherent (sometime even the apparent) optical properties could be estimated using Chl alone (Morel 1988; Morel and Maritorena 2001). However, as shown in Højerslev et al. (1991) and Morel et al. (2007) for various oceanic waters, significantly different relationships between K_d(UV) and K_d(visible) or between K_d(UV) and Chl exist; thus, such a scheme to predict K_d(UV) from one variable runs into difficulties for the global ocean. To highlight this difficulty, Figure 13 shows scatterplots between K_d(360), K_d(380) and K_d(490), respectively, where the R^2 values are ~0.8 even for the waters with bottom depth deeper than 1,000 m. For R_{rs} of global oceans, the R^2 values are ~0.89 between R_{rs}(360), R_{rs}(380) and R_{rs}(440) obtained from the VIIRS (see Figure 14). These patterns clearly indicate that not all R_{rs}(nbUV) or K_d(nbUV) of oceanic waters can be accurately predicted from R_{rs}(440) or K_d(490), respectively. This further echoes that oceanic waters are not necessarily "Case 1" (IOCCG 2000; Lee and Hu 2006); thus, a scheme to estimate R_{rs} or K_d in the UV domain based on the "Case 1" assumption may result in large uncertainties.

4.5 Consistency of R_{rs}(UV) among SeaWIFS, MODIS, and VIIRS

Following the same deep-learning approach, $UVISR_{dl}$ systems were developed for the spectral bands of SeaWiFS and MODIS (which is certainly also possible for other satellites after adjusting $UVISR_{dl}$ accordingly). It is then interesting to see if the R_{rs}(nbUV) products from these satellites are consistent. Observations by SeaWiFS and MODIS (Aqua) are overlapped between 2002 and 2010; observations by MODIS (Aqua) and VIIRS (SNPP) are overlapped from 2012 onward. We thus picked October to December in 2005 to compare SeaWIFS and MODIS and used October to December in 2012 to compare MODIS and VIIRS. The unbiased relative difference (URD) of R_{rs}(nbUV) between two satellite sensors is calculated to evaluate the consistency, with URD defined as:

$$\mathrm{URD} = \frac{\mathrm{Sensor_2} - \mathrm{MODIS}}{\mathrm{Sensor_2} + \mathrm{MODIS}} \times 2, \tag{5}$$

where $\mathrm{Sensor_2}$ is either for SeaWiFS or VIIRS.

Figure 15 (*a*, *c*, *e*) shows the global distributions of URD calculated between MODIS and VIIRS R_{rs}(nbUV); Figure 15 (*b*, *d*, *f*) shows the histograms of URD at each nbUV band; and Figure 16a presents scatterplots of R_{rs}(nbUV) between VIIRS and MODIS at 360 nm. We can see that R_{rs}(nbUV) from the two pairs of sensors agree with each other very well, where the URD values are generally around 0 in the tropical and subtropical regions, but higher near the polar regions and many coastal areas (e.g., west coast of India). This higher value reflects the strong spatial variation of coastal water properties and different spatial and temporal coverages of these satellite sensors. The average URD(360) is -0.017, with R^2 value as 0.95, and the slope is close to 1.0 in the linear regression (see Figure 16*a*). These measures are similar to those at 440 nm (see Figure 16*b*), both being independent measurements. Furthermore, Figures 16*c* and 16*d* compare the $R_{rs}(360)$ and $R_{rs}(440)$ between SeaWiFS and MODIS, demonstrating similar statistical measures at 360 nm and 440 nm, which is parallel to the comparison between MODIS and VIIRS. These evaluations indicate highly consistent R_{rs}(nbUV) among these satellite ocean color measurements, as long as R_{rs}(visible) is consistent among them.

5. Summary and future perspectives

To fill the data gap of UV penetration in the global ocean, especially for measurements after the launch and operation of modern ocean color satellites, a deep-learning-based system ($\mathrm{UVISR_{dl}}$) is developed to estimate R_{rs} at the near-blue UV bands (specifically at 360, 380, and 400 nm in this study) with R_{rs} in the visible (410-670 nm) as the input. We show that $\mathrm{UVISR_{dl}}$-estimated R_{rs}(nbUV) agree very well (<10% difference) with those from radiometric measurements, although larger differences are found between VIIRS R_{rs}(nbUV) and matchup *in situ* data when measurements were taken in coastal regions. With estimated R_{rs}(nbUV) and known R_{rs}(visible) of the global oceans from ocean color satellites, K_d(nbUV-visible) of the global oceans can then be calculated semi-analytically; thus, penetration of radiation in the nbUV domain in the global oceans can be clearly characterized through the combination of UV radiation products at the ocean surface. Such information will be useful for a broad range of biogeochemical studies. In addition, the availability of R_{rs}(nbUV) can help both atmospheric correction and decomposition of the total absorption coefficient into its components.

This study is an initial step to estimate R_{rs}(nbUV), using a deep-learning scheme, from R_{rs} at the available visible bands of ocean color satellites, where its evaluation is still limited. It is important and necessary to evaluate R_{rs}(nbUV) obtained by UVISR$_{dl}$, and subsequently K_d(nbUV) with more inclusive global measurements to obtain a comprehensive characterization and understanding of UVISR$_{dl}$ for ocean color satellites. Some current ocean color satellites, e.g., the OLCI, SGLI, and HY1C, and other planned future ocean color satellites, e.g., the PACE, cover a few bands in the 350-400 nm range. It will thus be valuable to evaluate R_{rs}(nbUV) obtained from UVISR$_{dl}$ by comparing to R_{rs}(nbUV) measured directly by satellites, although both determination has its own uncertainties. While R_{rs}(nbUV) from UVISR$_{dl}$ should not be considered as a means to replace R_{rs}(nbUV) from satellite measurements at the nbUV bands, it nevertheless can be an important data source to fill the data gaps in the past and present and a data source when atmospheric correction runs into difficulties in the nbUV bands.

Acknowledgments:

Financial support by the Chinese Ministry of Science and Technology through the National Key Research and Development Program of China (#2016YFC1400904) and the National Natural Science Foundation of China (#41941008, #41890803, and #41830102), the Joint Polar Satellite System (JPSS) funding for the NOAA ocean color calibration and validation (Cal/Val) project, and the University of Massachusetts Boston is greatly appreciated. We are grateful to the MOBY team for providing the *in situ* data in support of various satellite ocean color missions. We thank NASA OBPG for processing and providing global SeaWiFS and MODIS ocean color data, and colleagues for sharing field measurements via NASA SeaBASS. We also thank three anonymous reviewers for constructive comments and suggestions. The views, opinions, and findings contained in this paper are those of the authors and should not be construed as an official NOAA or U.S. Government position, policy, or decision.

References

Abadi, M., Barham, P., Chen, J., Chen, Z., Davis, A., Dean, J., Devin, M., Ghemawat, S., Irving, G., & Isard, M. (2016). TensorFlow: a system for large-scale machine learning. *operating systems design and implementation*, 265-283.

Antoine, D., d'Ortenzio, F., Hooker, S.B., Bécu, G., Gentili, B., Tailliez, D., & Scott, A.J. (2008). Assessment of uncertainty in the ocean reflectance determined by three satellite ocean color sensors (MERIS, SeaWiFS and MODIS‐A) at an offshore site in the Mediterranean Sea (BOUSSOLE project). *Journal of Geophysical Research: Oceans, 113*, doi:10.1029/2007JC004472.

Austin, R.W., & Petzold, T.J. (Year). Spectral dependence of the diffuse attenuation coefficient of light in ocean waters: a reexamination using new data. *Ocean Optics X*, 79-93.

Bricaud, A., Morel, A., & Prieur, L. (1981). Absorption by Dissolved Organic Matter of the Sea (Yellow Substance) in the UV and Visible Domains. *Limnology and Oceanography, 26*, 43-53.

Cao, F., Fichot, C.G., Hooker, S.B., & Miller, W.L. (2014). Improved algorithms for accurate retrieval of UV/visible diffuse attenuation coefficients in optically complex, inshore waters. *Remote Sensing of Environment, 144*, 11-27.

Chollet, F. (2015). keras. *https://github.com/fchollet/keras*.

Clark, D., Gordon, H., Voss, K., Ge, Y., Broenkow, W., & Trees, C. (1997). Validation of atmospheric correction over the oceans. *Journal of Geophysical Research: Atmospheres, 102*, 17209-17217.

Conde, D., Aubriot, L., & Sommaruga, R. (2000). Changes in UV penetration associated with marine intrusions and freshwater discharge in a shallow coastal lagoon of the Southern

Atlantic Ocean. *Marine Ecology Progress Series, 207*, 19-31.

Craig, S.E., Lee, Z., & Du, K. (2020). Top of Atmosphere, Hyperspectral Synthetic Dataset for PACE (Phytoplankton, Aerosol, and ocean Ecosystem) Ocean Color Algorithm Development. In: PANGAEA, https://doi.org/10.1594/PANGAEA.915747.

Cullen, J.J., & Neale, P.J. (1994). Ultraviolet radiation, ozone depletion, and marine photosynthesis. *Photosynthesis Research, 39*, 303-320.

Dupouy, C., Frouin, R., Tedetti, M., Maillard, M., Rodier, M., & Lombard, F. (2018). Diazotrophic Trichodesmium influence on ocean color and pigment composition in the South West tropical Pacific. *Biogeosciences*, 15, 5249-5269.

Dupouy, C., Neveux, J., & André, J.-M. (1997). Spectral absorption coefficient of photosynthetically active pigments in the equatorial Pacific Ocean (165° 11–150° W). *Deep Sea Research Part II: Topical Studies in Oceanography, 44*, 1881-1906.

Fichot, C.G., Sathyendranath, S., & Miller, W.L. (2008). SeaUV and SeaUVC: Algorithms for the retrieval of UV/Visible diffuse attenuation coefficients from ocean color. *Remote Sensing of Environment, 112*, 1584-1602.

Frouin, R.J., Franz, B.A., Ibrahim, A., Knobelspiesse, K., Ahmad, Z., Cairns, B., Chowdhary, J., Dierssen, H.M., Tan, J., & Dubovik, O. (2019). Atmospheric correction of satellite ocean-color imagery during the PACE era. *Frontiers in earth science, 7*, 145.

Gao, B.-C., Li, R.-R., Lucke, R.L., Davis, C.O., Bevilacqua, R.M., Korwan, D.R., Montes, M.J., Bowles, J.H., & Corson, M.R. (2012). Vicarious calibrations of HICO data acquired from the International Space Station. *Applied Optics, 51*, 2559-2567.

Géron, A. (2019). *Hands-on machine learning with Scikit-Learn, Keras, and TensorFlow: Concepts, tools, and techniques to build intelligent systems*. O'Reilly Media.

Gordon, H.R. (1989a). Can the Lambert‐Beer law be applied to the diffuse attenuation coefficient of ocean water? *Limnology and Oceanography, 34*, 1389-1409.

Gordon, H.R. (1989b). Dependence of the diffuse reflectance of natural waters on the sun angle. *Limnology and Oceanography, 34*, 1484-1489.

Gordon, H.R., Brown, O.B., Evans, R.H., Brown, J.W., Smith, R.C., Baker, K.S., & Clark, D.K. (1988). A semianalytic radiance model of ocean color. *Journal of Geophysical Research: Atmospheres, 93*, 10909-10924.

Gordon, H.R., & Morel, A. (1983). *Remote assessment of ocean color for interpretation of satellite visible imagery: A review*. New York: Springer-Verlag.

He, K., Zhang, X., Ren, S., & Sun, J. (Year). Delving deep into rectifiers: Surpassing human-level performance on imagenet classification. *Proceedings of the IEEE international conference on computer vision*, 1026-1034.

He, X., Bai, Y., Pan, D., Tang, J., & Wang, D. (2012). Atmospheric correction of satellite ocean color imagery using the ultraviolet wavelength for highly turbid waters. *Optics Express, 20*, 20754-20770.

Herman, J., & Celarier, E. (1997). Earth surface reflectivity climatology at 340–380 nm from TOMS data. *Journal of Geophysical Research: Atmospheres, 102*, 28003-28011.

Højerslev, N., & Aas, E. (1991). A relationship for the penetration of ultraviolet B radiation into the Norwegian Sea. *Journal of Geophysical Research: Oceans, 96*, 17003-17005.

Hu, C., Lee, Z., & Franz, B. (2012). Chlorophyll aalgorithms for oligotrophic oceans: A novel approach based on three - band reflectance difference. *Journal of Geophysical Research: Oceans, 117*, doi:10.1029/2011JC007395, 002012.

IOCCG-OCAG (2003). Model, parameters, and approaches that used to generate wide range of absorption and backscattering spectra. In: International Ocean Colour Coordinating Group, http://www.ioccg.org/groups/OCAG_data.html.

IOCCG (2000). Remote Sensing of Ocean Colour in Coastal, and Other Optically-Complex, Waters. In S. Sathyendranath (Ed.), *Reports of the International Ocean-Colour Coordinating Group, No.3*. Dartmouth, Canada: IOCCG.

IOCCG (2006). Remote Sensing of Inherent Optical Properties: Fundamentals, Tests of Algorithms, and Applications. In Z.-P. Lee (Ed.), *Reports of the International Ocean-Colour Coordinating Group, No. 5* (p. 126). Dartmouth, Canada: IOCCG.

IOCCG (2010). Atmospheric Correction for Remotely-Sensed Ocean-Colour Products. In M. Wang (Ed.), *Reports of the International Ocean-Colour Coordinating Group* (p. 83). Dartmouth, Canada: IOCCG.

Kahn, R.A., Sayer, A.M., Ahmad, Z., & Franz, B.A. (2016). The sensitivity of SeaWiFS ocean color retrievals to aerosol amount and type. *Journal of Atmospheric and Oceanic Technology, 33*, 1185-1209.

Kahru, M., & Mitchell, B.G. (1998). Spectral reflectance and absorption of a massive red tide off southern California. *Journal of Geophysical Research: Oceans, 103*, 21601-21609.

Ketkar, N. (2017). *Introduction to Keras*. Apress.

Kingma, D.P., & Ba, J. (2014). Adam: A method for stochastic optimization. *arXiv preprint arXiv:1412.6980.*

Krizhevsky, A., Sutskever, I., & Hinton, G.E. (Year). Imagenet classification with deep convolutional neural networks. *Advances in neural information processing systems*, 1097-1105.

Kuchinke, C., Fienberg, K., & Nunez, M. (2004). The angular distribution of UV-B sky radiance under cloudy conditions: a comparison of measurements and radiative transfer calculations using a fractal cloud model. *Journal of Applied Meteorology, 43*, 751-761.

Lee, Z., Carder, K.L., & Arnone, R.A. (2002). Deriving inherent optical properties from water color: a multiband quasi-analytical algorithm for optically deep waters. *Applied Optics, 41*, 5755-5772.

Lee, Z., & Hu, C. (2006). Global distribution of Case-1 waters: An analysis from SeaWiFS measurements. *Remote Sensing of Environment, 101*, 270-276.

Lee, Z., Hu, C., Shang, S., Du, K., Lewis, M., Arnone, R., & Brewin, R. (2013). Penetration of UV - visible solar radiation in the global oceans: Insights from ocean color remote sensing. *Journal of Geophysical Research: Oceans, 118*, 4241-4255.

Lee, Z., Shang, S., Hu, C., & Zibordi, G. (2014). Spectral interdependence of remote-sensing reflectance and its implications on the design of ocean color satellite sensors. *Applied Optics, 53*, 3301-3310.

Lee, Z., Wei, J., Voss, K., Lewis, M., Bricaud, A., & Huot, Y. (2015a). Hyperspectral absorption coefficient of "pure" seawater in the range of 350–550 nm inverted from remote sensing reflectance. *Applied Optics, 54*, 546-558.

Lee, Z., Wei, J., Voss, K., Lewis, M., Bricaud, A., & Huot, Y. (2015b). Hyperspectral absorption coefficient of "pure" seawater in the range of 350–550 nm inverted from remote sensing reflectance. *Applied Optics, 54*, 546-558.

Lee, Z.P., Carder, K.L., & Du, K.P. (2004). Effects of molecular and particle scatterings on model parameters for remote-sensing reflectance. *Applied Optics, 43*, 4957-4964.

Lee, Z.P., Du, K.P., & Arnone, R. (2005). A model for the diffuse attenuation coefficient of downwelling irradiance. *Journal of Geophysical Research: Oceans, 110*, doi:10.1029/2004JC002275.

Lin, H., Lee, Z., Lin, G., & Yu, X. (2020). Experimental evaluation of the self-shadow and its correction for on-water measurements of water-leaving radiance. *Applied Optics, 59*, 5325-5334.

Mannino, A., Russ, M.E., & Hooker, S.B. (2008). Algorithm development and validation for satellite‐derived distributions of DOC and CDOM in the US Middle Atlantic Bight. *Journal of Geophysical Research: Oceans, 113*, doi:10.1029/2007JC004493.

Mason, J.D., Cone, M.T., & Fry, E.S. (2016). Ultraviolet (250–550 nm) absorption spectrum of pure water. *Appl. Opt., 55*, 7163.

Mélin, F., Sclep, G., Jackson, T., & Sathyendranath, S. (2016). Uncertainty estimates of remote sensing reflectance derived from comparison of ocean color satellite data sets. *Remote Sensing of Environment, 177*, 107-124.

Moisan, T., & Mitchell, B. (2001). UV absorption by mycosporine-like amino acids in Phaeocystis antarctica Karsten induced by photosynthetically available radiation. *Marine Biology, 138*, 217-227.

Morel, A. (1988). Optical modeling of the upper ocean in relation to its biogenous matter content (case I waters). *Journal of Geophysical Research: Oceans, 93*, 10749-10768.

Morel, A., Claustre, H., Antoine, D., & Gentili, B. (2007). Natural variability of bio-optical properties in Case 1 waters: attenuation and reflectance within the visible and near-UV spectral domains, as observed in South Pacific and Mediterranean waters. *Biogeosciences, 4*, 913-925.

Morel, A., & Gentili, B. (2009). A simple band ratio technique to quantify the colored dissolved and detrital organic material from ocean color remotely sensed data. *Remote Sensing of Environment, 113*, 998-1011.

Morel, A., & Maritorena, S. (2001). Bio‐optical properties of oceanic waters: A reappraisal. *Journal of Geophysical Research: Oceans, 106*, 7163-7180.

Morel, A., & Prieur, L. (1977). Analysis of variations in ocean color. *Limnology and Oceanography, 22*, 709-722.

Morrison, J.R., & Nelson, N.B. (2004). Seasonal cycle of phytoplankton UV absorption at the Bermuda Atlantic Time‐series Study (BATS) site. *Limnology and Oceanography, 49*, 215-224.

Overmans, S., & Agustí, S. (2019). Latitudinal gradient of UV attenuation along the highly transparent Red Sea Basin. *Photochemistry and photobiology, 95*, 1267-1279.

Piccini, C., Conde, D., Pernthaler, J., & Sommaruga, R. (2009). Alteration of chromophoric dissolved organic matter by solar UV radiation causes rapid changes in bacterial community composition. *Photochemical & Photobiological Sciences, 8*, 1321-1328.

Pope, R., & Fry, E. (1997). Absorption spectrum (380 - 700 nm) of pure waters: II. Integrating cavity measurements. *Applied Optics, 36*, 8710-8723.

Rose, K.C., Williamson, C.E., Fischer, J.M., Connelly, S.J., Olson, M., Tucker, A.J., & Noe, D.A. (2012). The role of ultraviolet radiation and fish in regulating the vertical distribution ofDaphnia. *Limnology and Oceanography, 57*, 1867-1876.

Sathyendranath, S., Lazzara, L., & Prieur, L. (1987). Variations in the spectral values of specific absorption of phytoplankton. *Limnology and Oceanography, 32*, 403-415.

Shick, J.M., & Dunlap, W.C. (2002). Mycosporine-like amino acids and related gadusols: biosynthesis, accumulation, and UV-protective functions in aquatic organisms. *Annual review of Physiology, 64*, 223-262.

Siegel, D.A., Maritorena, S., Nelson, N.B., & Behrenfeld, M.J. (2005). Independence and interdependencies among global ocean color properties: Reassessing the bio‐optical assumption. *Journal of Geophysical Research: Oceans, 110*, doi:10.1029/2004JC002527.

Smith, R.C., & Baker, K.S. (1981). Optical properties of the clearest natural waters. *Applied Optics, 20*, 177-184.

Smith, R.C., Prezelin, B., Baker, K.e.a., Bidigare, R., Boucher, N., Coley, T., Karentz, D., MacIntyre, S., Matlick, H., & Menzies, D. (1992). Ozone depletion: ultraviolet radiation and phytoplankton biology in Antarctic waters. *science, 255*, 952-959.

Smyth, T. (2011a). Penetration of UV irradiance into the global ocean. *Journal of Geophysical Research: Oceans, 116*

Smyth, T.J. (2011b). Penetration of UV irradiance into the global ocean. *Journal of Geophysical Research: Oceans, 116*, doi:10.1029/2011JC007183.

Steiner, B., Devito, Z., Chintala, S., Gross, S., Paszke, A., Massa, F., Lerer, A., Chanan, G., Lin, Z., & Yang, E. (Year). PyTorch: An Imperative Style, High-Performance Deep Learning Library. *neural information processing systems*, 8026-8037.

Sun, D., Hu, C., Qiu, Z., & Wang, S. (2015). Reconstruction of hyperspectral reflectance for optically complex turbid inland lakes: test of a new scheme and implications for inversion algorithms. *Optics Express, 23*, A718-A740.

Swami, A., & Jain, R. (2011). Scikit-learn: Machine Learning in Python. *Journal of Machine Learning Research, 12*, 2825-2830.

Swan, C.M., Nelson, N.B., Siegel, D.A., & Fields, E.A. (2013). A model for remote estimation of ultraviolet absorption by chromophoric dissolved organic matter based on the global distribution of spectral slope. *Remote Sensing of Environment, 136*, 277-285.

Tanaka, A., Sasaki, H., & Ishizaka, J. (2006). Alternative measuring method for water-leaving radiance using a radiance sensor with a domed cover. *Optics Express, 14*, 3099-3105.

Tedetti, M., Charrière, B., Bricaud, A., Para, J., Raimbault, P., & Sempéré, R. (2010). Distribution of normalized water‐leaving radiances at UV and visible wave bands in relation with chlorophyll a and colored detrital matter content in the southeast Pacific. *Journal of Geophysical Research: Oceans, 115*, doi:10.1029/2009JC005289.

Tedetti, M., & Sempéré, R. (2006). Penetration of ultraviolet radiation in the marine environment. A review. *Photochemistry and photobiology, 82*, 389-397.

Twardowski, M.S., Boss, E., Sullivan, J.M., & Donaghay, P.L. (2004). Modeling the spectral shape of absorption by chromophoric dissolved organic matter. *Marine Chemistry, 89*, 69-88.

Vantrepotte, V., & Mélin, F. (2006). UV penetration in the water column EUR 22217. *Institute for Environment and Sustainability, European Commission Directorate General Joint Research Centre. Luxembourg: European Communities*

Vasilkov, A., Krotkov, N., Herman, J., McClain, C., Arrigo, K., & Robinson, W. (2001). Global mapping of underwater UV irradiances and DNA‐weighted exposures using Total Ozone Mapping Spectrometer and Sea‐viewing Wide Field‐of‐view Sensor data products. *Journal of Geophysical Research: Oceans, 106*, 27205-27219.

Vasilkov, A.P., Herman, J.R., Ahmad, Z., Kahru, M., & Mitchell, B.G. (2005). Assessment of the ultraviolet radiation field in ocean waters from space-based measurements and full radiative-transfer calculations. *Applied Optics, 44*, 2863-2869.

Vernet, M., & Whitehead, K. (1996). Release of ultraviolet-absorbing compounds by the red-tide dinoflagellateLingulodinium polyedra. *Marine Biology, 127*, 35-44.

Wang, M. (2007). Remote sensing of the ocean contributions from ultraviolet to near-infrared using the shortwave infrared bands: simulations. *Applied Optics, 46*, 1535-1547.

Wang, M., & Jiang, L. (2018). Atmospheric correction using the information from the short blue band. *IEEE Transactions on Geoscience and Remote Sensing, 56*, 6224-6237.

Wang, M., Son, S., & Harding Jr, L.W. (2009). Retrieval of diffuse attenuation coefficient in the Chesapeake Bay and turbid ocean regions for satellite ocean color applications. *Journal of Geophysical Research: Oceans, 114*

Wei, J., & Lee, Z. (2015). Retrieval of phytoplankton and colored detrital matter absorption coefficients with remote sensing reflectance in an ultraviolet band. *Applied Optics, 54*, 636-649.

Wei, J., Lee, Z., Ondrusek, M., Mannino, A., Tzortziou, M., & Armstrong, R. (2016). Spectral slopes of the absorption coefficient of colored dissolved and detrital material inverted from UV‐visible remote sensing reflectance. *Journal of Geophysical Research: Oceans, 121*, 1953-1969.

Wei, J., Yu, X., Lee, Z., Wang, M., & Jiang, L. (2020). Improving low-quality satellite remote sensing reflectance at blue bands over coastal and inland waters. *Remote Sensing of Environment, 250*, 112029.

Werdell, P.J., & Bailey, S.W. (2005). An improved in-situ bio-optical data set for ocean color algorithm development and satellite data product validation. *Remote Sensing of Environment, 98*, 122-140.

Werdell, P.J., Franz, B.A., Bailey, S.W., Feldman, G.C., Boss, E., Brando, V.E., Dowell, M., Hirata, T., Lavender, S.J., & Lee, Z. (2013). Generalized ocean color inversion model for retrieving marine inherent optical properties. *Applied Optics, 52*, 2019-2037.

Werdell, P.J., McKinna, L.I., Boss, E., Ackleson, S.G., Craig, S.E., Gregg, W.W., Lee, Z., Maritorena, S., Roesler, C.S., & Rousseaux, C.S. (2018). An overview of approaches and challenges for retrieving marine inherent optical properties from ocean color remote sensing. *Progress in Oceanography, 160*, 186-212.

Zeiler, M.D. (2012). Adadelta: an adaptive learning rate method. *arXiv preprint arXiv:1212.5701*.

Zepp, R., Erickson Iii, D., Paul, N., & Sulzberger, B. (2007). Interactive effects of solar UV radiation and climate change on biogeochemical cycling. *Photochemical & Photobiological Sciences, 6*, 286-300.

Zhang, X., & Hu, L. (2009a). Estimating scattering of pure water from density fluctuation of the refractive index. *Optics Express, 17*, 1671-1678.

Zhang, X.D., & Hu, L.B. (2009b). Estimating scattering of pure water from density fluctuation of the refractive index. *Optics Express, 17*, 1671-1678.

Zibordi, G., Berthon, J.-F., Mélin, F., D'Alimonte, D., & Kaitala, S. (2009). Validation of satellite ocean color primary products at optically complex coastal sites: Northern Adriatic Sea, Northern Baltic Proper and Gulf of Finland. *Remote Sensing of Environment, 113*, 2574-2591.

Zibordi, G., & Talone, M. (2020). On the equivalence of near-surface methods to determine the water-leaving radiance. *Optics Express, 28*, 3200-3214.

Appendix A:

To train $\mathrm{UVISR_{dl}}$, we created a large synthetic dataset covering wide ranges of inherent optical parameters (IOPs) and remote sensing reflectance (R_{rs}). The generation of this dataset generally follows the IOCCG Report 5 (IOCCG-OCAG 2003; IOCCG 2006) for synthesizing wide ranges of IOPs spectra, but an analytical model (Lee et al., 2004) was used to calculate R_{rs} from these IOPs, as generating such a large dataset with the Hydrolight software will take too long. However, this R_{rs} model was developed based on Hydrolight simulations where the accuracy is within ~1% on average, so the error of using an analytical formula for R_{rs} on the deep-learning system of this study is negligible.

Following the description in IOCCG-OCAG (2003), the absorption (a) and backscattering (b_b) coefficients, the two key component IOPs for R_{rs}, are modeled as

$$a(\lambda) = a_w(\lambda) + a_{ph}(\lambda) + a_{dm}(\lambda) + a_g(\lambda). \quad \text{(A1a)}$$

$$b_b(\lambda) = b_{bw}(\lambda) + b_{bph}(\lambda) + b_{bdm}(\lambda). \quad \text{(A1b)}$$

Here subscripts "w, ph, dm, g" represent pure seawater, phytoplankton pigments, detritus and minerals, and gelbstoff (e.g., CDOM), respectively.

Values of $a_w(\lambda)$ were taken from combinations of the literature. Specifically, a_w values of 350-550 nm are from Lee et al. (2015b), 551-725 nm from Pope and Fry (1997), 726-800 nm from Smith and Baker (1981). From more than 4,000 measured $a_{ph}(\lambda)$ spectra (350-800 nm, 5 nm step), 720 $a_{ph}(\lambda)$ spectra were selected with $a_{ph}(440)$ in a range of ~0.001-39.0 $\mathrm{m^{-1}}$, thus covering oceanic waters to waters with phytoplankton blooms.

Following the practice taken by the IOCCG-OCAG (2003), a_{dm} and a_g were modeled as

$$a_{dm}(\lambda) = a_{dm}(440)e^{-S_{dm}(\lambda-440)}, \quad \text{(A2a)}$$

$$a_g(\lambda) = a_g(440)e^{-S_g(\lambda-440)}, \quad \text{(A2b)}$$

where the slope parameters S_{dm} (~0.007-0.015 $\mathrm{nm^{-1}}$) and S_g (~0.01 - 0.02 $\mathrm{nm^{-1}}$) were taken as random values as in IOCCG-OCAG (2003), and $a_{dm}(440)$ and $a_g(440)$ were modeled as

$$a_{dm}(440) = p_1 \times a_{ph}(440), \quad \text{(A3a)}$$

$$a_g(440) = p_2 \times a_{ph}(440). \quad \text{(A3b)}$$

Parameters p_1 and p_2 were controlled random values, generating reasonable $a_{dm}(440)$ and $a_g(440)$ values for a given $a_{ph}(440)$ (IOCCG-OCAG 2003).

Values of $b_{bw}(\lambda)$ were taken from the literature (Zhang and Hu 2009b). Spectra of b_{bph} were also modeled as in IOCCG-OCAG (2003), where b_{bph} is aa

$$b_{bph}(\lambda) = B_{ph}(c_{ph}(\lambda) - a_{ph}(\lambda)), \quad \text{(A4a)}$$

$$c_{ph}(\lambda) = p_3 \times c_{ph}(550)(\frac{550}{\lambda})^{p_4}, \quad \text{(A4b)}$$

and B_{ph} is the backscattering ratio of phytoplankton and a value of 1% was taken. Parameters p_3 and p_4 were random values within given ranges as in IOCCG-OCAG (2003). Similarly, spectra of b_{bdm} were modeled as

$$b_{bdm}(\lambda) = 0.0183 p_5 \times b_{dm}(550)(\frac{550}{\lambda})^{p_6}, \quad \text{(A5)}$$

with p_5 and p_6 also random values within given ranges.

The relationship between r_{rs} and IOPs from Lee et al. (2004) was employed:

$$r_{\mathrm{rs}}(\lambda) = \mathrm{g}_w \frac{b_{\mathrm{bw}}(\lambda)}{a(\lambda) + b_{\mathrm{b}}(\lambda)} + \mathrm{g}_p \frac{b_{\mathrm{bp}}(\lambda)}{a(\lambda) + b_{\mathrm{b}}(\lambda)}, \quad \text{(A6a)}$$

$$\mathrm{g}_p(\lambda) = \mathrm{G}_0 \left[1 - \mathrm{G}_1 \exp\left(-\mathrm{G}_2 \frac{b_{\mathrm{bp}}(\lambda)}{a(\lambda) + b_{\mathrm{b}}(\lambda)}\right)\right], \quad \text{(A6b)}$$

Here g_{w} is the model parameter related to molecular scattering, and g_p is the model parameter related to particle-scattering phase function, and values of $G_{0\text{-}2}$ are constants for a given light geometry and particle phase function. $R_{rs}(\lambda)$ can be computed from $r_{rs}(\lambda)$ (Gordon et al. 1988) with a relationship as

$$R_{rs}(\lambda) = \frac{0.52 \ r_{rs}(\lambda)}{1 - 1.7 \ r_{rs}(\lambda)}. \quad \text{(A7)}$$

In the above system for the calculation of R_{rs}, a_{ph} is a free variable, while parameters p_1-p_6 are determined randomly in constrained ranges for each a_{ph}. The generation of these constrained random values followed that in IOCCG-OCAG (2003), and described in Craig et al. (2020). The 720 $a_{ph}(\lambda)$ spectra were divided into 12 groups, with each group having its own $a_{ph}(440)$ range. These $a_{ph}(\lambda)$ spectra were normalized to its $a_{ph}(440)$ to obtain a_{ph} spectral shapes. Total of 200,000 $a_{ph}(\lambda)$ were then generated by multiplying $a_{ph}(440)$ to these spectral shapes, with $a_{ph}(440)$ randomly varying in a range of 0.001-20.0 m^{-1}, while the spectral shapes were selected based on the $a_{ph}(440)$ value. Subsequently 200,000 groups of hyperspectral $a(\lambda)$&$b_b(\lambda)$ were generated following Eqs. A1-A5, and then 200,000 hyperspectral R_{rs} spectra were generated with Eqs. A6-A7, where the resulted $R_{rs}(550)$ is in a range of ~0.0008-0.090 sr^{-1}.

Table Captions:

Table 1. Range of remote sensing reflectance (taking $R_{rs}(555)$ as an example) used for evaluation of $UVISR_{dl}$. CV is the ratio of standard deviation to the mean.

Table 2. Statistical measures of $UVISR_{dl}$ after being applied to both synthetic and field measured datasets.

Table 3. Statistical measures between matchup VIIRS and measured R_{rs}. N is the number of matchup measurements.

Figure Captions:

Fig. 1. Schematic chart of the deep-learning-based system for estimating R_{rs}(nbUV) using R_{rs}(visible): UVISR$_{dl}$.

Fig. 2. Examples of R_{rs} spectra used in this study: (*a*) synthesized R_{rs} spectra for the development and validation of UVISR$_{dl}$, and (*b*) measured R_{rs} spectra to evaluate UVISR$_{dl}$.

Fig. 3. Comparison between R_{rs}(nbUV) and UVISR$_{dl}$-predicted R_{rs}(nbUV) of the synthetic dataset: (*a*) R_{rs}(360), (*b*) R_{rs}(380), and (*c*) R_{rs}(400).

Fig. 4. Relationship between R_{rs}(nbUV) and R_{rs}(440) of both synthetic and measured (SBA and MOBY) datasets: (*a*) R_{rs}(360) vs R_{rs}(440), (*b*) R_{rs}(380) vs R_{rs}(440), and (*c*) R_{rs}(400) vs R_{rs}(440).

Fig. 5. Comparison between R_{rs}(nbUV) and UVISR$_{dl}$-predicted R_{rs}(nbUV) of the measured SBA dataset: (*a*) R_{rs}(360), (*b*) R_{rs}(380), and (*c*) R_{rs}(400).

Fig. 6. Comparison between R_{rs}(nbUV) and UVISR$_{dl}$-predicted R_{rs}(nbUV) of the measured MOBY dataset: (*a*) R_{rs}(360), (*b*) R_{rs}(380), and (*c*) R_{rs}(400).

Fig. 7. Global distribution of seasonal composite R_{rs}(nbUV) for the period of October to December 2012 obtained from VIIRS: (*a*) R_{rs}(360), (*b*) R_{rs}(380) (white star showing measurements during November 2004), (*c*) R_{rs}(400), and (*d*) R_{rs}(410).

Fig. 8. Same as Fig. 7, except for showing R_{rs}(360) of three coastal regions.

Fig. 9. Locations of matchup field measurements (SBA and MOBY) to evaluate R_{rs}(nbUV) from VIIRS.

Fig. 10. Comparison between VIIRS and field measurements SBA R_{rs}: (*a*) R_{rs}(360), (*b*)

$R_{rs}(380)$, (*c*) $R_{rs}(400)$, (*d*) $R_{rs}(410)$, (*e*) $R_{rs}(440)$, and (*f*) $R_{rs}(490)$.

Fig. 11. Comparison between VIIRS and field measurements MOBY R_{rs}: (*a*) $R_{rs}(360)$, (*b*) $R_{rs}(380)$, (*c*) $R_{rs}(400)$, (*d*) $R_{rs}(410)$, (*e*) $R_{rs}(440)$, and (*f*) $R_{rs}(490)$.

Fig. 12. Global distribution of seasonal composite K_d(nbUV) for the period of October to December 2012 obtained from VIIRS: (*a*) $K_d(360)$, and (*b*) $K_d(380)$.

Fig. 13. Relationships between K_d(nbUV) and $K_d(490)$ of global waters obtained from VIIRS: (*a*) $K_d(360)$ vs $K_d(490)$, and (*b*) $K_d(380)$ vs $K_d(490)$. Color dots are for bottom depth > 1,000 m, and gray dots, for bottom depth < 1,000 m. The R^2 values are for the data with depth > 1,000 m.

Fig. 14. Same as Fig. 13, except between R_{rs}(nbUV) and $R_{rs}(440)$: (*a*) $R_{rs}(360)$ vs $R_{rs}(440)$, and (*b*) $R_{rs}(380)$ vs $R_{rs}(440)$. Color dots are for data with bottom depth > 1,000 m, and gray points for data with bottom depth < 1,000 m.

Fig. 15. Global distribution (left) and histogram (right) of URD(nbUV) between MODIS and VIIRS for seasonal data of October–December 2012: (a) 360 nm, (b) 380 nm, and (c) 400 nm.

Fig. 16. Comparison of R_{rs} between MODIS and VIIRS (*a, b*), and between MODIS and SeaWiFS (*c, d*).

Table 1. Range of remote sensing reflectance (taking R_{rs}(555) as an example) used for evaluation of UVISR$_{dl}$. CV is the ratio of standard deviation to the mean.

Data	Data Sources (Data Number)	Band	Min (sr^{-1})	Max (sr^{-1})	Mean (sr^{-1})	CV
Training data	Synthetic data (160,000)	R_{rs}(555)	7.7×10^{-4}	0.091	0.016	0.85
Validation data	Synthetic data (40,000)		7.8×10^{-4}	0.089	0.019	0.84
	SBA data (202)		1.1×10^{-3}	0.020	0.0048	0.84
	MOBY (6,184)		8.1×10^{-4}	$3.3*10^{-3}$	0.0013	0.086

Table 2. Statistical measures of $UVISR_{dl}$ after being applied to both synthetic and field measured datasets.

(a): Synthetic dataset

Data (Data Number)	Sensor	Band	RMSD (sr^{-1})	MARD	bias (sr^{-1})	MAURD	R^2
Synthetic data (40,000)	SeaWiFS	360	1.1×10^{-4}	2.3×10^{-3}	2.3×10^{-6}	0.023	>0.99
		380	5.7×10^{-5}	1.7×10^{-3}	3.8×10^{-7}	0.015	>0.99
		400	1.2×10^{-5}	7.6×10^{-4}	1.2×10^{-6}	0.0075	>0.99
	MODIS	360	1.1×10^{-4}	2.6×10^{-3}	-2.2×10^{-7}	0.026	>0.99
		380	5.3×10^{-5}	1.4×10^{-3}	-3.8×10^{-7}	0.015	>0.99
		400	1.2×10^{-5}	3.7×10^{-4}	4.0×10^{-7}	0.0038	>0.99
	VIIRS	360	$1.0*10^{-4}$	2.5×10^{-3}	5.0×10^{-6}	0.024	>0.99
		380	5.9×10^{-5}	1.5×10^{-3}	-1.3×10^{-6}	0.015	>0.99
		400	1.4×10^{-5}	6.2×10^{-4}	1.4×10^{-6}	0.006	>0.99

(b): Field dataset

Data (Data Number)	Sensor	Band	RMSD (sr^{-1})	MARD	bias (sr^{-1})	MAURD	R^2
SBA data (202)	SeaWiFS	360	3.4×10^{-4}	0.098	1.1×10^{-4}	0.094	>0.98
		380	2.2×10^{-4}	0.041	-1.8×10^{-5}	0.041	>0.99
		400	8.6×10^{-5}	0.015	2.8×10^{-5}	0.015	>0.99
	MODIS	360	3.3×10^{-4}	0.085	7.7×10^{-5}	0.082	>0.98
		380	2.1×10^{-4}	0.045	-8.7×10^{-6}	0.045	>0.99
		400	8.8×10^{-5}	0.020	-5.8×10^{-5}	0.020	>0.99
	VIIRS	360	3.5×10^{-4}	0.095	1.2×10^{-5}	0.091	>0.98
		380	2.1×10^{-4}	0.041	-1.5×10^{-5}	0.042	>0.99
		400	8.3×10^{-5}	0.015	-4.7×10^{-5}	0.015	>0.99
MOBY data (6184)	SeaWiFS	360	1.1×10^{-3}	0.076	9.0×10^{-4}	0.072	>0.88
		380	6.1×10^{-4}	0.038	4.6×10^{-4}	0.037	>0.96
		400	1.8×10^{-4}	0.011	5.7×10^{-5}	0.011	>0.99
	MODIS	360	1.2×10^{-3}	0.083	9.9×10^{-4}	0.078	>0.87
		380	5.6×10^{-4}	0.035	4.1×10^{-4}	0.034	>0.95
		400	1.9×10^{-4}	0.012	9.4×10^{-5}	0.012	>0.99
	VIIRS	360	1.2×10^{-3}	0.085	1.0×10^{-3}	0.081	>0.87
		380	6.0×10^{-4}	0.038	4.3×10^{-4}	0.037	>0.95
		400	1.9×10^{-4}	0.011	7.8×10^{-5}	0.011	>0.99

Table 3. Statistical measures between matchup VIIRS and measured R_{rs}. N is the number of matchup measurements.

Field data	Band	N	RMSD (sr^{-1})	MARD	bias (sr^{-1})	MAURD	R^2
SBA	360	82	0.0016	0.48	0.0005	0.40	0.74
	380		0.0015	0.39	0.0004	0.34	0.77
	400		0.0013	0.33	0.0002	0.31	0.80
	410		0.0012	0.30	0.0002	0.29	0.82
	440		0.0011	0.23	-0.00008	0.25	0.82
	490		0.0013	0.18	-0.0004	0.21	0.80
MOBY	360	730	0.0023	0.14	1.2×10^{-3}	0.13	0.25
	380		0.0022	0.13	9.2×10^{-4}	0.12	0.26
	400		0.0019	0.12	2.3×10^{-4}	0.12	0.23
	410		0.0017	0.11	-3.2×10^{-5}	0.11	0.22
	440		0.0013	0.11	-4.2×10^{-4}	0.11	0.17
	490		0.00082	0.11	-3.9×10^{-4}	0.12	0.06

Figures:

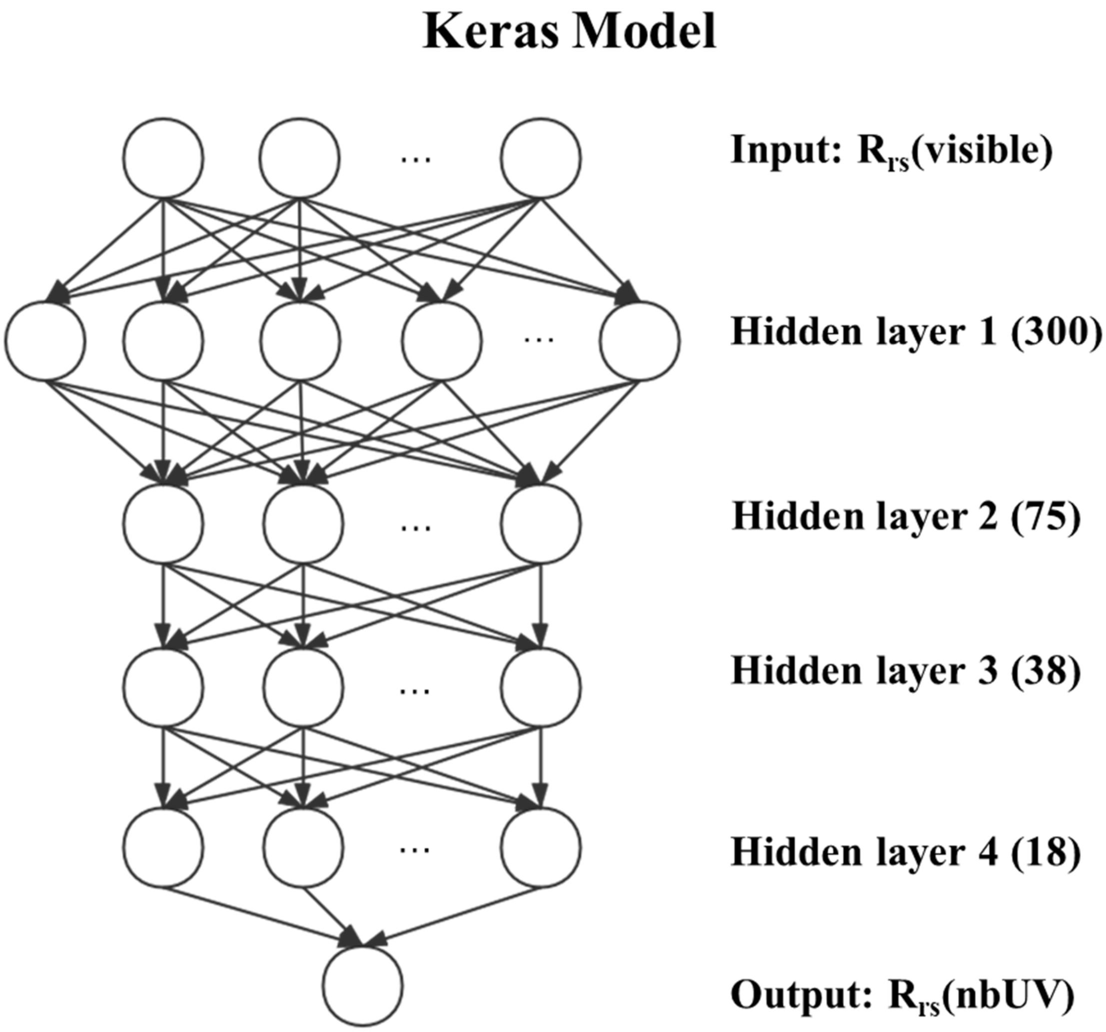

Fig. 1. Schematic chart of the deep-learning-based system for estimating R_{rs}(nbUV) using R_{rs}(visible): $\mathrm{UVISR_{dl}}$.

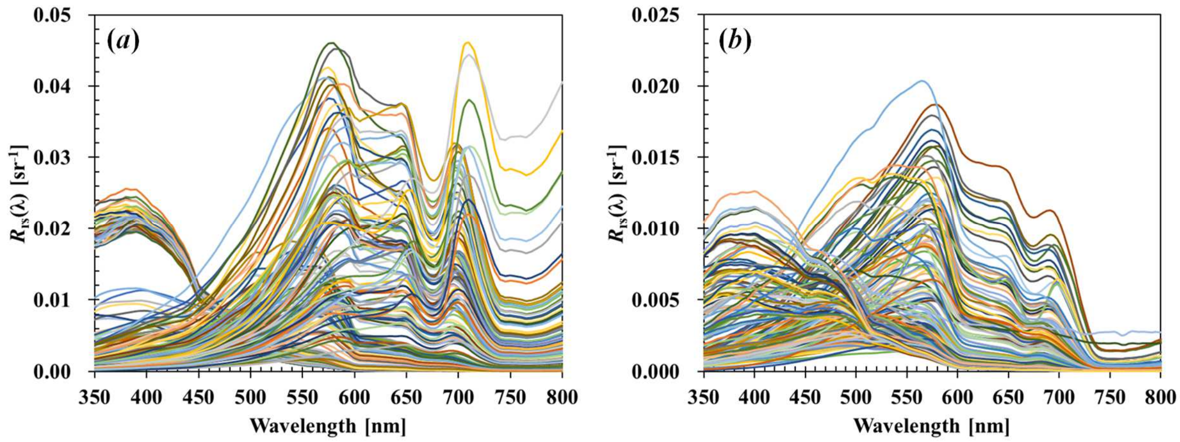

Fig. 2. Examples of R_{rs} spectra used in this study: (*a*) synthesized R_{rs} spectra for the development and validation of UVISR$_{dl}$, and (*b*) measured R_{rs} spectra to evaluate UVISR$_{dl}$.

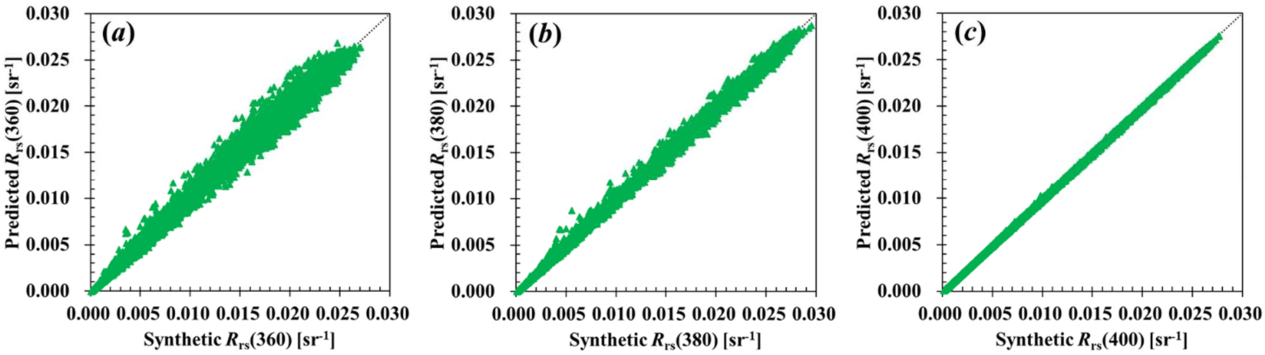

Fig. 3. Comparison between R_{rs}(nbUV) and UVISR$_{dl}$-predicted R_{rs}(nbUV) of the synthetic dataset: (*a*) R_{rs}(360), (*b*) R_{rs}(380), and (*c*) R_{rs}(400).

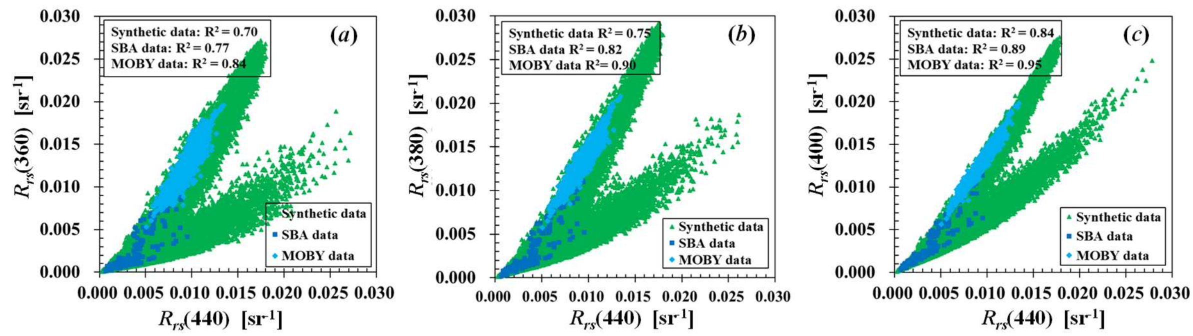

Fig. 4. Relationship between R_{rs}(nbUV) and R_{rs}(440) of both synthetic and measured (SBA and MOBY) datasets: (*a*) R_{rs}(360) vs R_{rs}(440), (*b*) R_{rs}(380) vs R_{rs}(440), and (*c*) R_{rs}(400) vs R_{rs}(440).

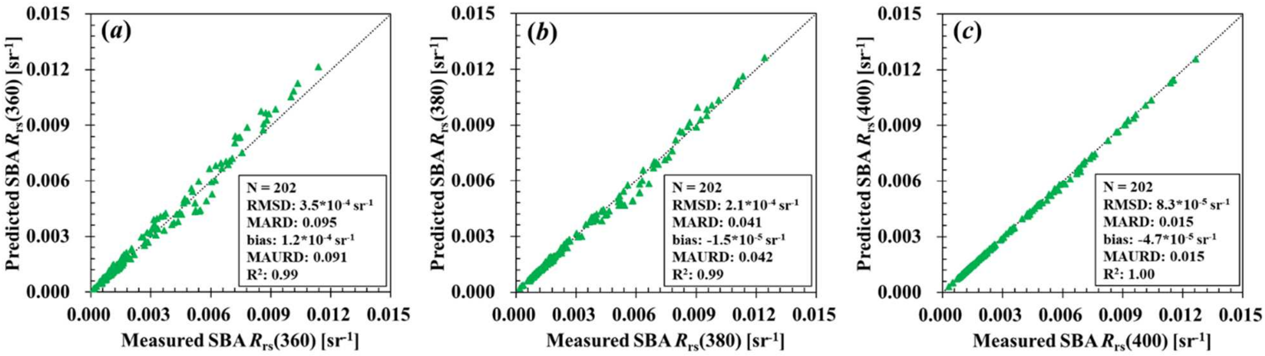

Fig. 5. Comparison between R_{rs}(nbUV) and UVISR$_{\mathrm{dl}}$-predicted R_{rs}(nbUV) of the measured SBA dataset: (*a*) R_{rs}(360), (*b*) R_{rs}(380), and (*c*) R_{rs}(400).

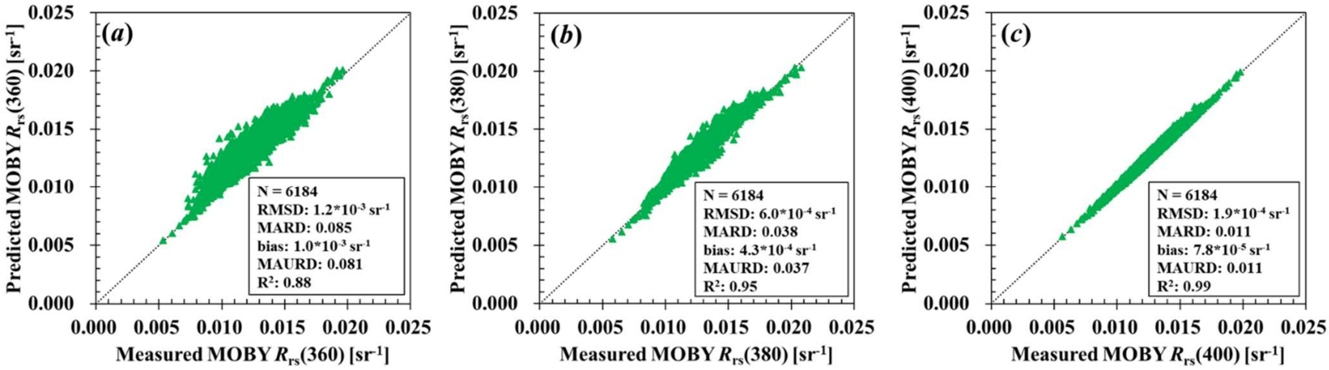

Fig. 6. Comparison between R_{rs}(nbUV) and UVISR$_{dl}$-predicted R_{rs}(nbUV) of the measured MOBY dataset: (*a*) R_{rs}(360), (*b*) R_{rs}(380), and (*c*) R_{rs}(400).

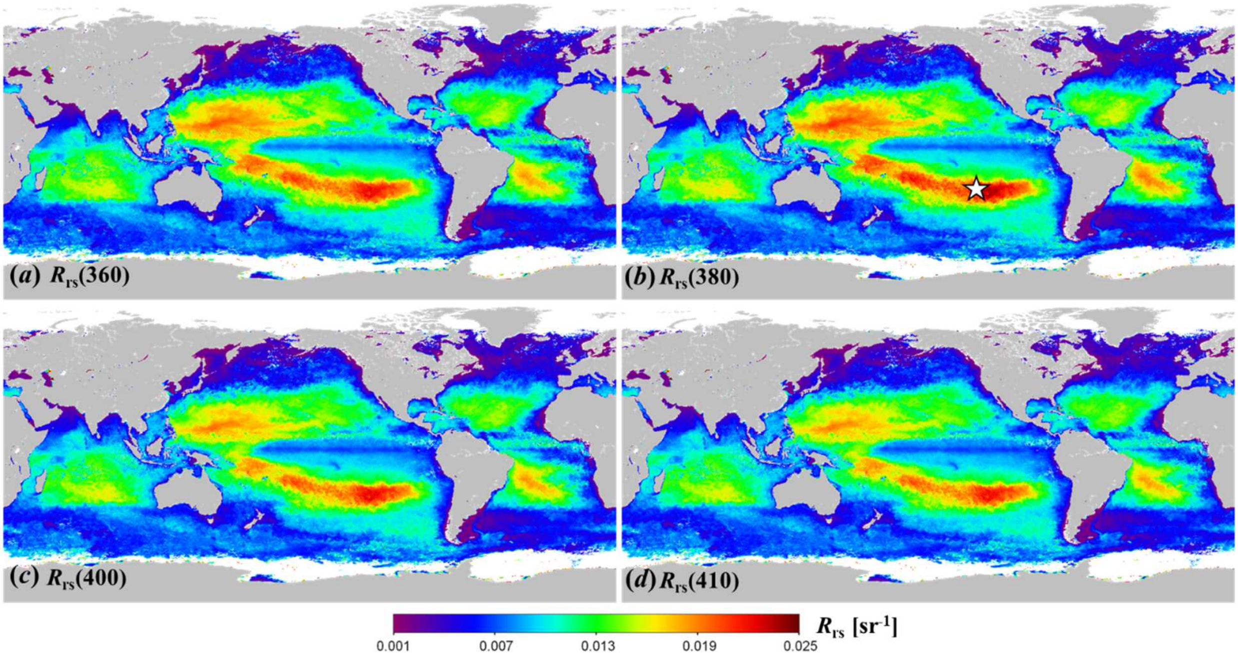

Fig. 7. Global distribution of seasonal composite R_{rs}(nbUV) for the period of October to December 2012 obtained from VIIRS: (*a*) $R_{rs}(360)$, (*b*) $R_{rs}(380)$ (white star showing measurements during November 2004), (*c*) $R_{rs}(400)$, and (*d*) $R_{rs}(410)$.

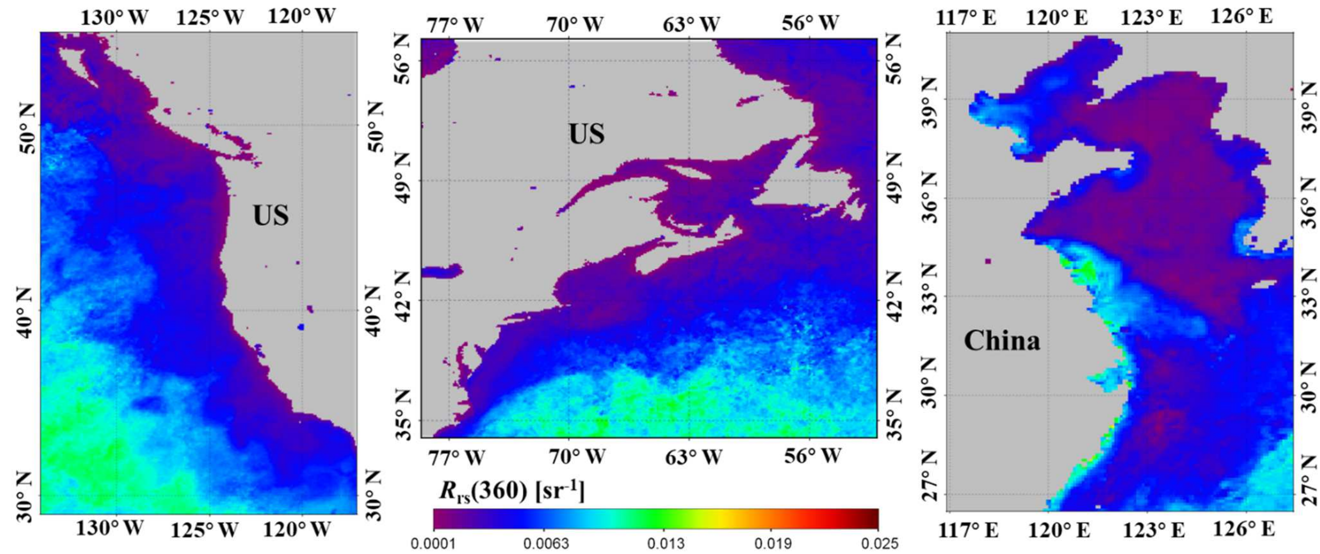

Fig. 8. Same as Fig. 7, except for showing $R_{rs}(360)$ of three coastal regions.

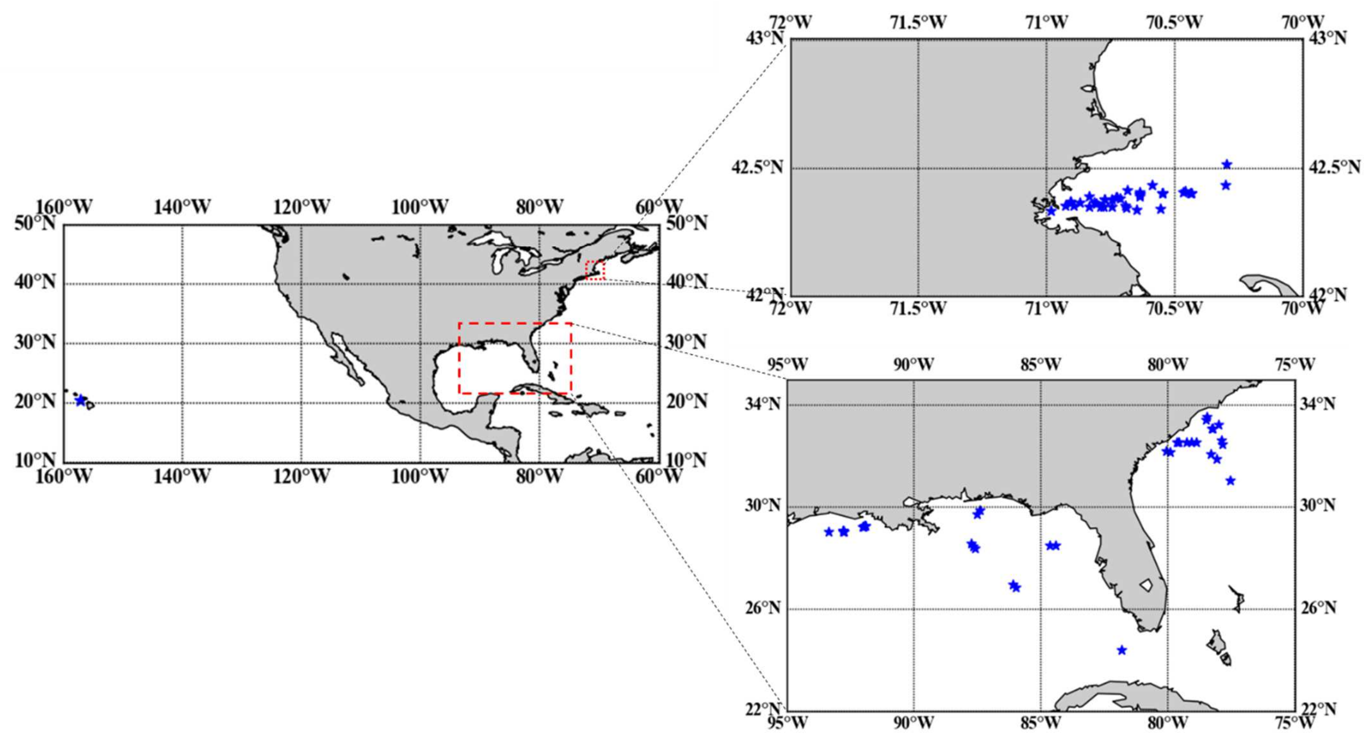

Fig. 9. Locations of matchup field measurements (SBA and MOBY) to evaluate R_{rs}(nbUV) from VIIRS.

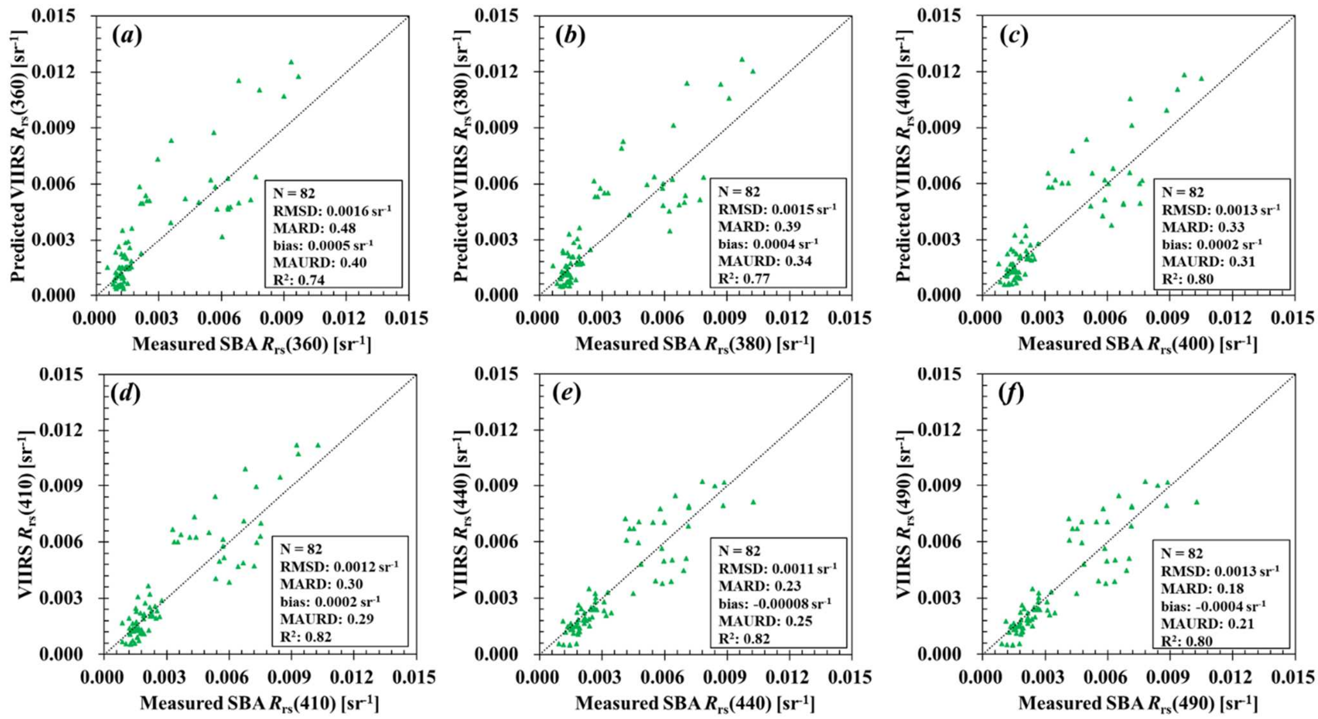

Fig. 10. Comparison between VIIRS and field measurements SBA R_{rs}: (*a*) R_{rs}(360), (*b*) R_{rs}(380), (*c*) R_{rs}(400), (*d*) R_{rs}(410), (*e*) R_{rs}(440), and (*f*) R_{rs}(490).

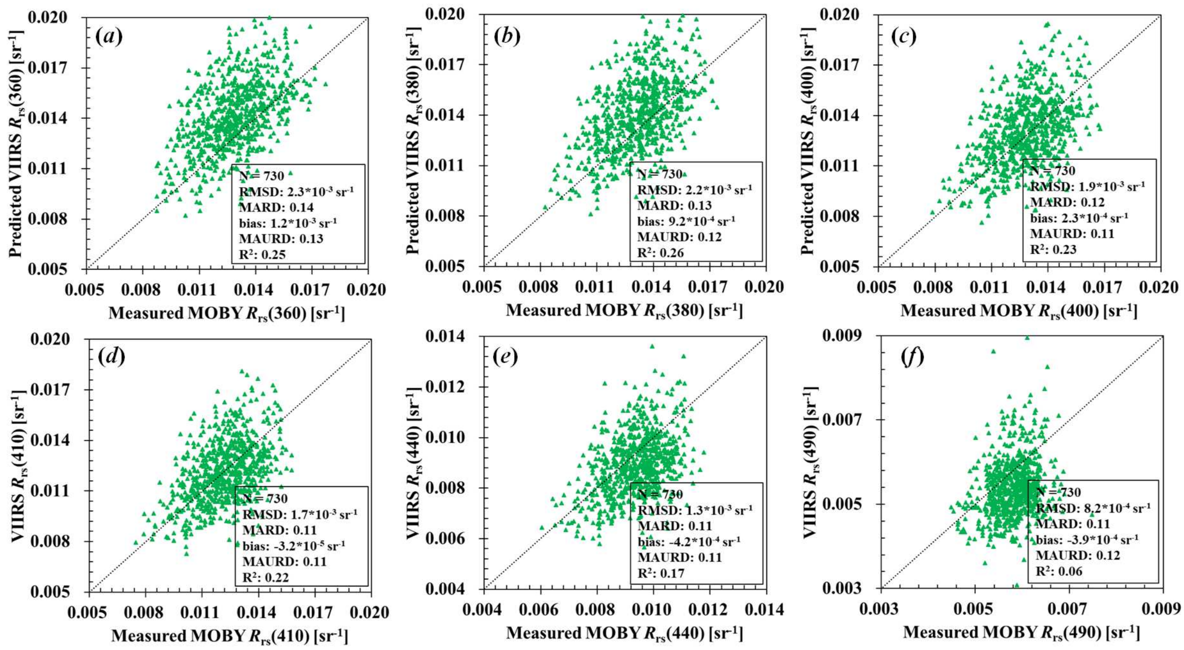

Fig. 11. Comparison between VIIRS and field measurements MOBY R_{rs}: (*a*) R_{rs}(360), (*b*) R_{rs}(380), (*c*) R_{rs}(400), (*d*) R_{rs}(410), (*e*) R_{rs}(440), and (*f*) R_{rs}(490).

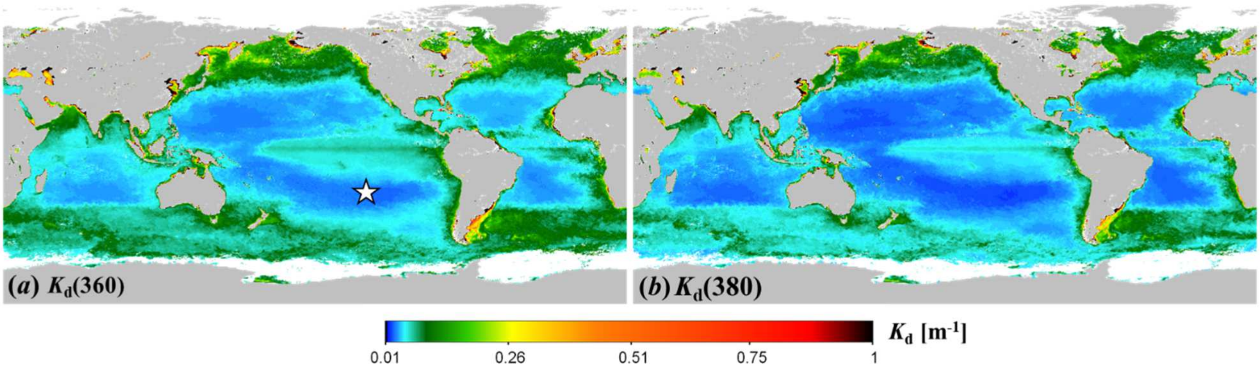

Fig. 12. Global distribution of seasonal composite K_d(nbUV) for the period of October to December 2012 obtained from VIIRS: (*a*) K_d(360), and (*b*) K_d(380).

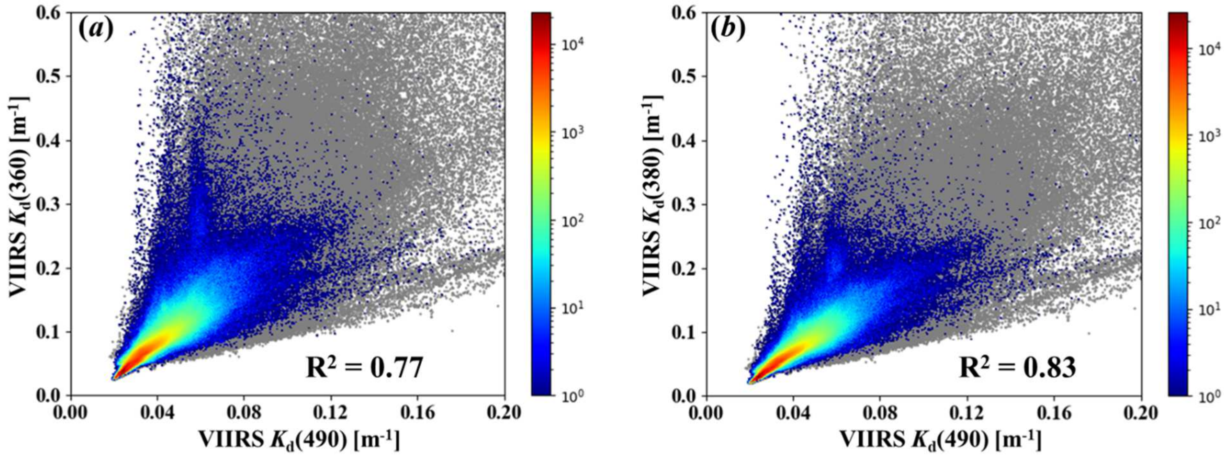

Fig. 13. Relationships between K_d(nbUV) and K_d(490) of global waters obtained from VIIRS: (*a*) K_d(360) vs K_d(490), and (*b*) K_d(380) vs K_d(490). Color dots are for bottom depth > 1,000 m, and gray dots, for bottom depth < 1,000 m. The R^2 values are for the data with depth > 1,000 m.

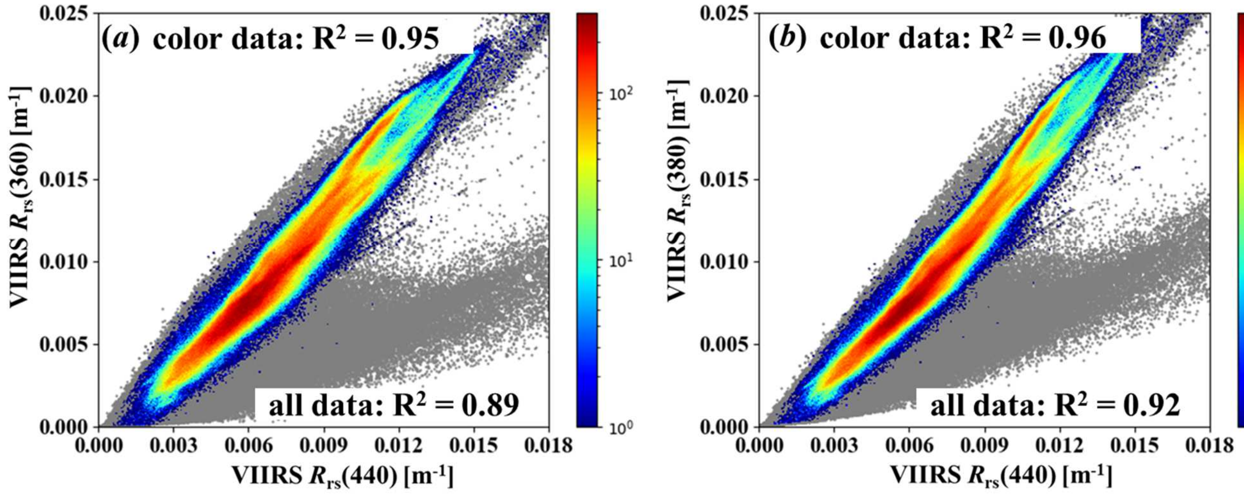

Fig. 14. Same as Fig. 13, except between R_{rs}(nbUV) and R_{rs}(440): (*a*) R_{rs}(360) vs R_{rs}(440), and (*b*) R_{rs}(380) vs R_{rs}(440). Color dots are for data with bottom depth > 1,000 m, and gray points for data with bottom depth < 1,000 m.

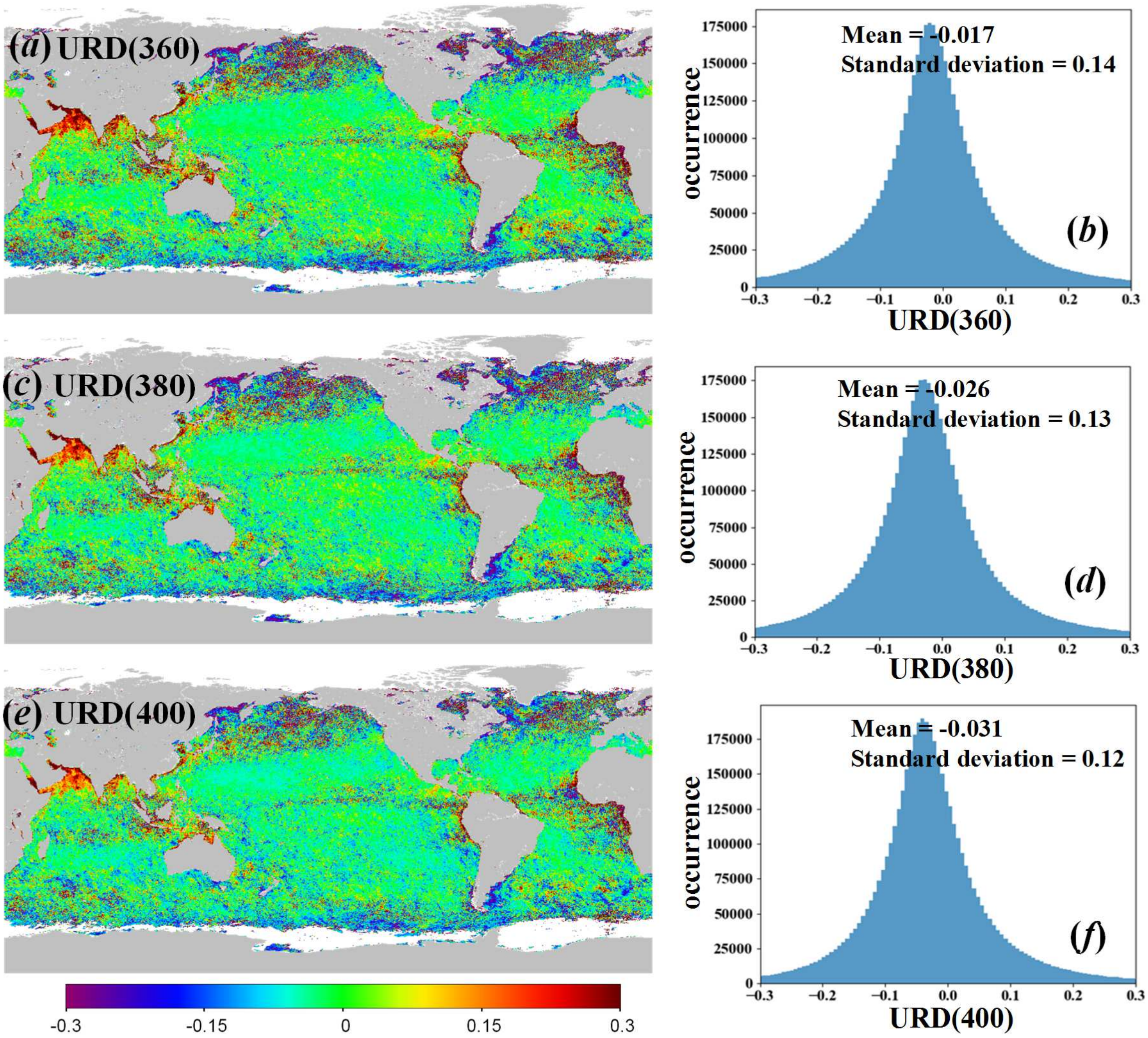

Fig. 15. Global distribution (left) and histogram (right) of URD(nbUV) between MODIS and VIIRS for seasonal data of October–December 2012: (a) 360 nm, (b) 380 nm, and (c) 400 nm.

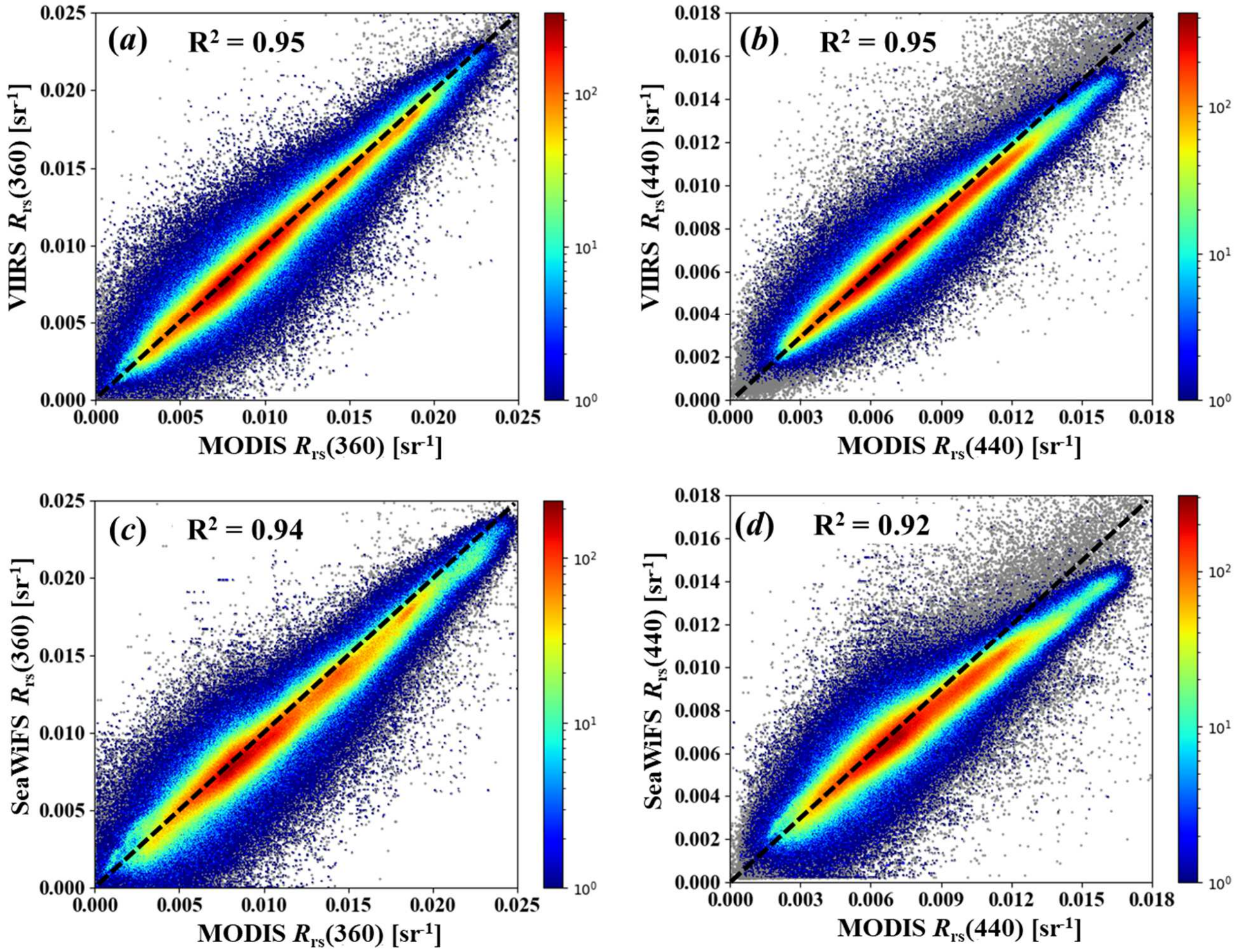

Fig. 16. Comparison of R_{rs} between MODIS and VIIRS (*a, b*), and between MODIS and SeaWiFS (*c, d*).